UNIVERSITÀ DEGLI STUDI DI BARI ALDO MORO

Dipartimento Interateneo di Fisica «M. Merlin»

DOTTORATO DI RICERCA IN FISICA

CICLO XXXVI

Settore Scientifico Disciplinare FIS/01

STUDY OF GAMMA RAYS PRODUCED BY THE INTERACTIONS OF COSMIC RAYS WITH SMALL SOLAR SYSTEM BODIES WITH THE FERMI LARGE AREA TELESCOPE

Dottorando:

Salvatore De Gaetano

Supervisori:

Dott. Mario Nicola Mazziotta

Dott. Fabio Gargano

Coordinatore:

Ch.mo Prof. Giuseppe Gonnella

Introduction

- All known asteroids have diameters > 2 m and the majority is distributed along the ecliptic plane
  - Asteroid sizes are inferred from optical observations

- They can be divided into three main families:
  - Main Belt Asteroids (all bodies between the orbits of Mars and Jupiter)
  - Trojans, which share an orbit with a larger planet or moon
  - Kuiper Belt Asteroids (Trans-Neptunian objects)

- Mainly made of carbon (C-type), silicate (S-type) and metal (M-type)

- They can be passive sources of gamma rays, produced by CRs impinging on them
  - Production of a diffuse gamma-ray emission along the ecliptic plane
  - Way to investigate asteroid properties: size distribution

- In this thesis work, the gamma-ray flux from the ecliptic plane has been studied by using *Fermi*-LAT data
  - The FLUKA code has been used to calculate the gamma-ray emission from asteroids with realistic composition and density values
  - Comparison between model and data: setting a constraint on the asteroid size distribution

SSSBs size distribution

- Based on the collisional story of asteroids, their population can be described by a power-law
- Assuming they are homogeneous spheres of radius r, one can write:

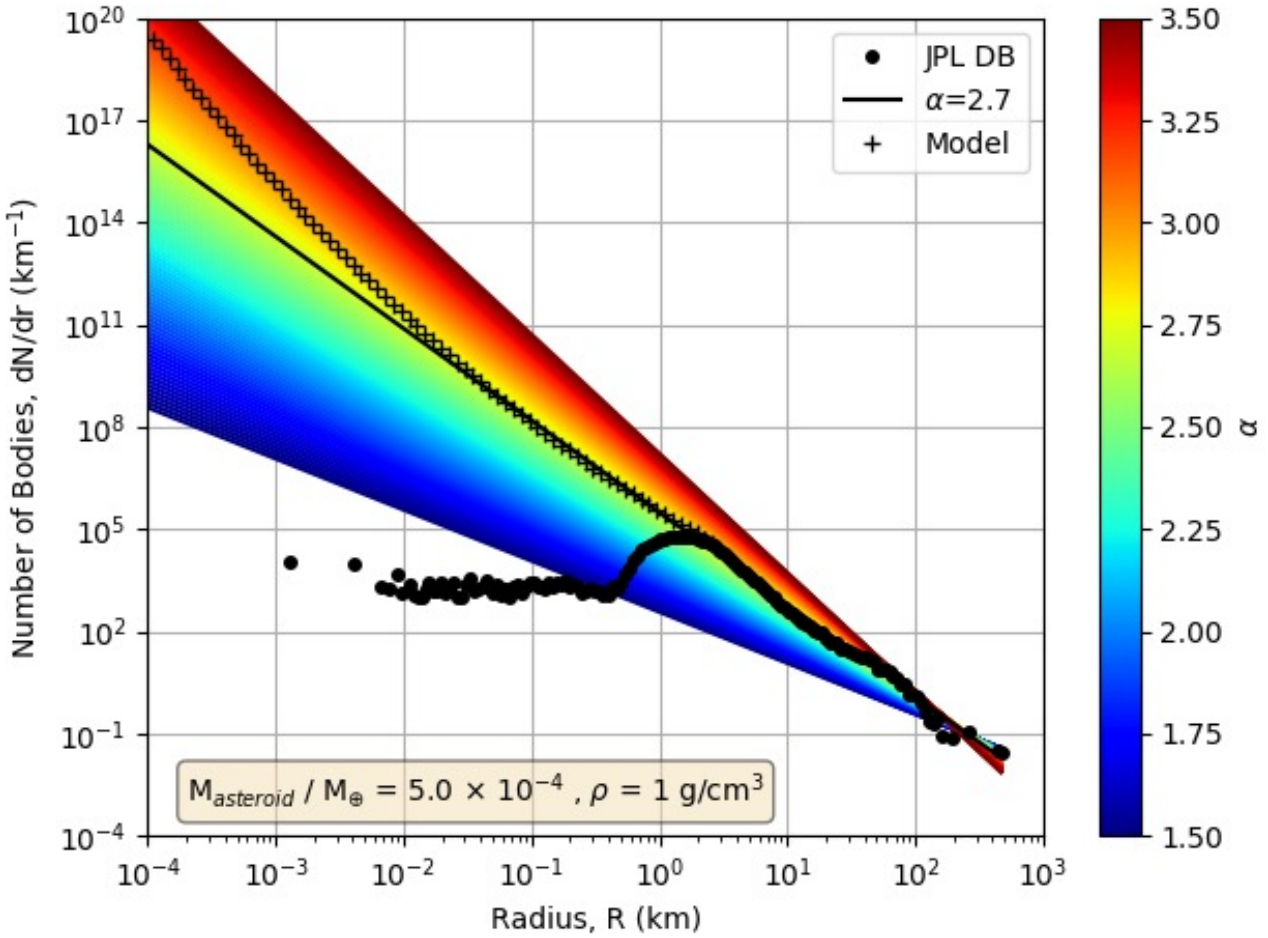

$$\frac{dN}{dr} = a\, r^{-\alpha} \qquad a = \begin{cases} \dfrac{3M}{4\pi\rho} \times \dfrac{4-\alpha}{r_1^{4-\alpha} - r_0^{4-\alpha}} & \text{for } \alpha \neq 4 \\ \dfrac{3M}{4\pi\rho} \times \dfrac{1}{\log \frac{r_1}{r_0}} & \text{for } \alpha = 4 \end{cases}$$

- The plot includes the size distribution from the JPL catalog
- Black crosses: extension to 10 cm of a size distribution model proposed by Durda et al. (1998)
- In this work, a size distribution model for SSSBs has been assumed
  - It follows the JPL catalog for $r > 1.25$ km, the extrapolated Durda et al. model for $10\ \text{cm} < r < 1.25\ \text{km}$

Differential gamma-ray flux from SSSBs

- Flux $(\mathrm{GeV}^{-1}\,\mathrm{cm}^{-2}\,\mathrm{s}^{-1})$ of gamma rays of energy E_γ from $N_{tot}(r)$ bodies in a sky pixel at spatial coordinates (λ, β), covering a solid angle $\Delta\Omega$:

Spectral factor

Spatial factor

$$\phi_\gamma(E_\gamma, r, \lambda, \beta) = \pi r^2 I_\gamma(E_\gamma, r) N_{tot}(r) \sum_{i \in l.o.s.} \frac{w(\lambda, \beta, d_i)}{\Delta\Omega\, d_i^2}$$

- $I_\gamma(E_\gamma, r)$ = gamma-ray intensity at the production site $(\mathrm{GeV}^{-1}\,\mathrm{cm}^{-2}\,\mathrm{sr}^{-1}\,\mathrm{s}^{-1})$
- $\omega(\lambda, \beta, d_i)$ = fraction of bodies at spatial coordinates (λ, β) and distance d_i from the Earth
  - The fraction $\frac{\omega(\lambda,\beta,d_i)}{\Delta\Omega\, d_i^2}$ is summed along the line-of-sight

If the spatial factor $\sum_{i \in l.o.s.} \frac{\omega(\lambda,\beta,d_i)}{\Delta\Omega\, d_i^2}$ and $I_\gamma(E_\gamma, r)$ are known or estimated, by fitting the LAT data with the model in the previous equation, it is possible to set constraints on $N_{tot}(r)$

Building the spatial map of SSSBs

- The fraction ω of asteroids in the coordinates (λ, β), covering a solid angle $\Delta\Omega$, at a distance d_i from the Earth, was obtained in three steps:
  - Extracting 10^7 times the parameters describing the asteroid orbits from the parameter distributions in the JPL catalog: 10^7 asteroid positions in terms of orbital parameters
  - Converting the obtained positions into positions in ecliptic coordinates
  - Estimating, for each extracted asteroid position, the corresponding distance d_i from the Earth by randomly extracting (uniformly) the Earth angular position on its orbit

- The sky was divided into 12288 pixels, each one covering a solid angle of $\Delta\Omega = 1.02 \times 10^{-3}$ sr
  - This was achieved using a HEALPix pixelization of the sky

- Each pixel was assigned a weight given by the spatial factor

$$\sum_{i \in l.o.s.} \frac{w(\lambda, \beta, d_i)}{\Delta\Omega\, d_i^2}$$

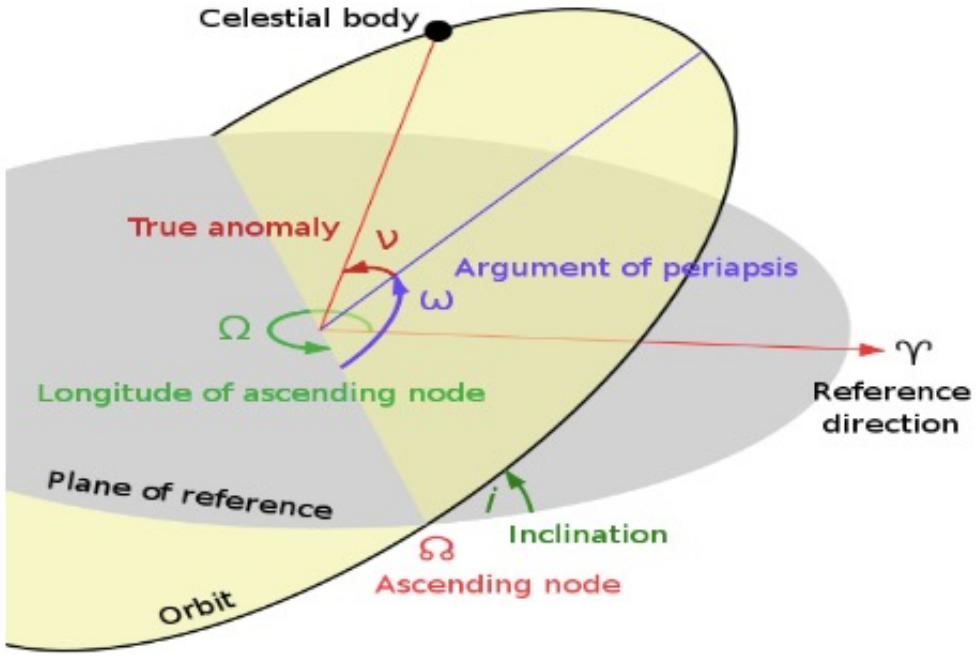

Wikipedia 2022

Building the spatial map of SSSBs

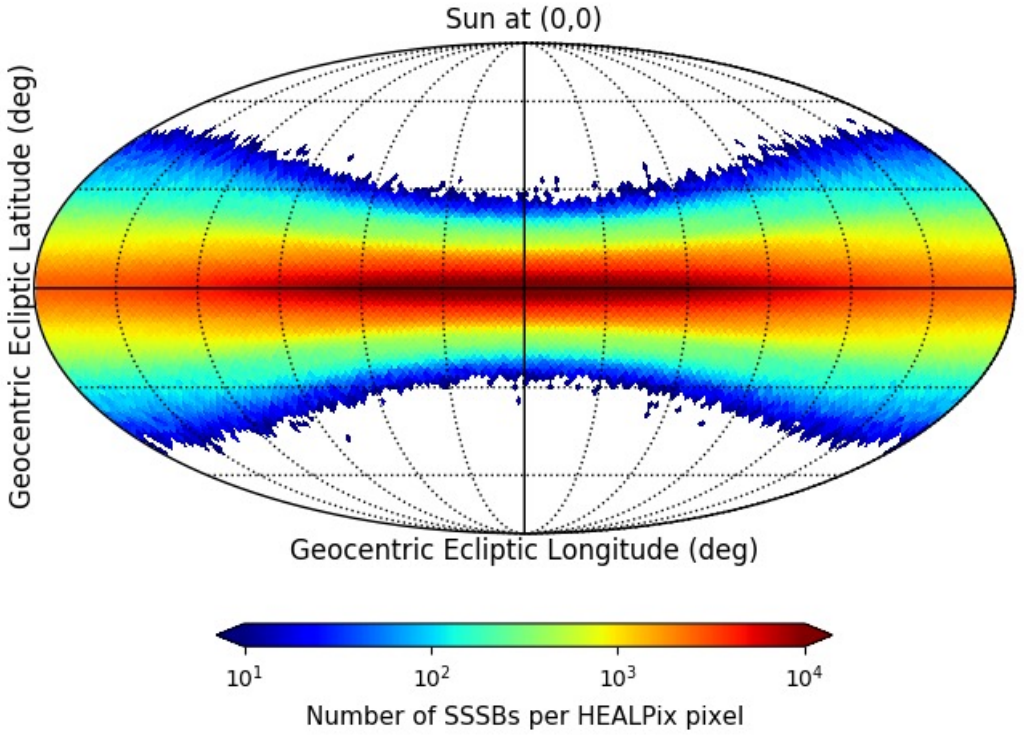

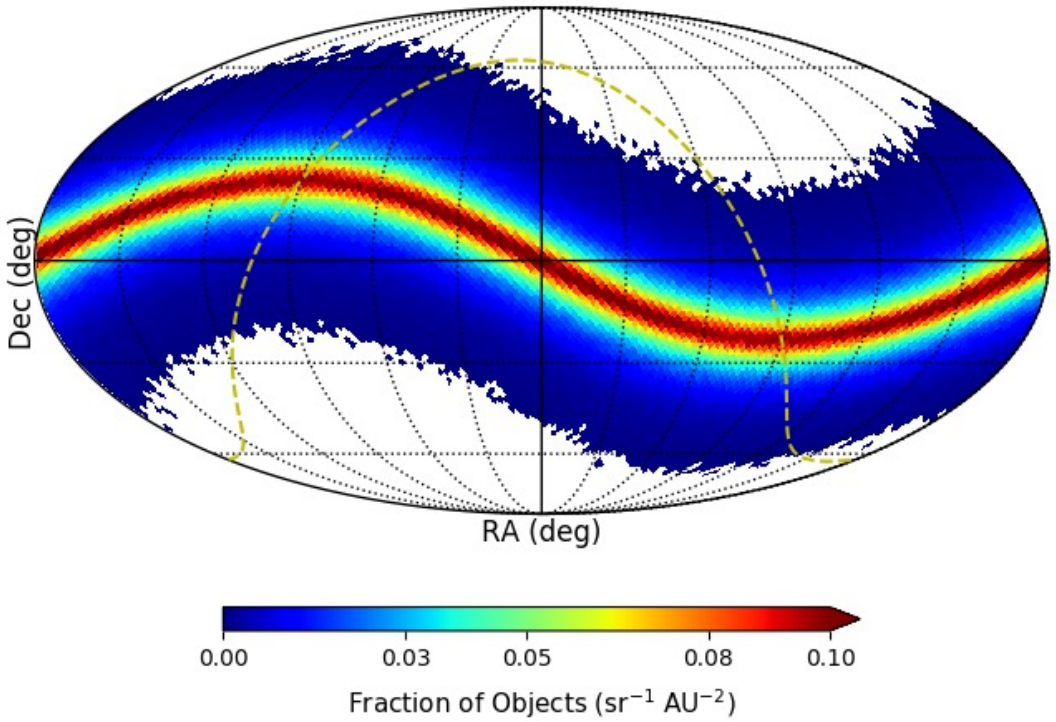

- Most asteroids are concentrated along the ecliptic plane
- The asteroid distribution is more narrowed toward the direction of the Sun
  - Projection effect: the asteroids along the Earth-Sun direction are, on average, farther from the Earth than those along the opposite direction

- The bright strip, along which the majority of bodies are concentrated, represents the ecliptic plane
- The dashed yellow line represents the Galactic plane in celestial coordinates
  - Ecliptic and Galactic plane intersect in two regions

Cosmic rays

- Cosmic rays (CRs) are energetic particles coming from the outer space
  - They are charged particles of energy up to 10^{20} eV
  - **Primary CRs:** particles directly produced and accelerated at the source
  - **Secondary CRs:** produced through interactions between primary CRs and any other object they meet in their journey towards the Earth

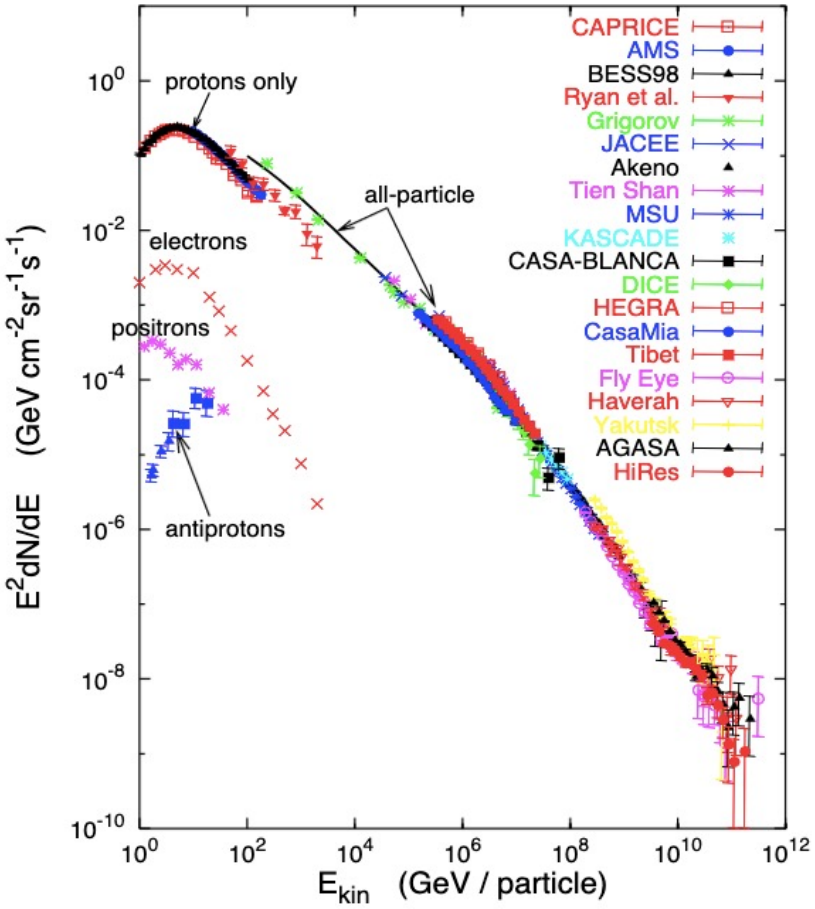

- For $E < 1\mathrm{GeV}$, the CR spectrum exhibits a cut-off, due to solar modulation
  - Interactions of low-energy CRs with the *solar wind*
  - The solar modulation has a cycle of 11 years
- For $E > 1\mathrm{GeV}$, up to a hundred EeV, the CR spectrum can be described by a power-law with index α depending on the energy range (α ≃ 2.7 up to 10^{15} eV, α ≃ 3 up to 3×10^{18} eV, then α ≃ 2.7)
- 98% of CRs are made of protons and nuclei
  - 87% protons, 12% helium, 1% heavier nuclei
- 2% of CRs are made of electrons

A. M. Hillas, 2006

Main mechanisms of production of gamma radiation

Interactions with matter

- Hadronic interactions: inelastic collisions of high-energy protons and nuclei with matter
  - At high energies, production of gamma rays mainly from neutral pions
- Bremsstrahlung: interactions of high-energy positrons or electrons with the Coulomb field of a nucleus
  - The energies of the emitted photons are distributed over a continuous spectrum
- Electron-positron annihilation in matter

Interactions with photons or radiation fields

- Inverse Compton scattering: a low-energy photon interacts with a high-energy electron/positron and gains energy at the expense of the electron/positron kinetic energy
- Synchrotron radiation: it is emitted when energetic electrons/positrons are bent in a circular orbit, for example due to the presence of a magnetic field

Gamma-ray intensity from asteroids

$$I_\gamma(E_\gamma, r) = \sum_i \int Y_i(E_\gamma | E_k, r) I_i(E_k) dE_k$$

- $Y_i(E_\gamma | E_k, r)$: yield (in units of GeV^{-1}) of gamma rays produced by the interaction of the *i*-th CR species with energy E_k with the body surface of radius r
- Yield calculated by performing simulations with the FLUKA code
  - Several samples of p, e^- and He nuclei were simulated with different kinetic energies, impinging on the SSSBs with a uniform and isotropic distribution
  - Each SSSB is a spherical body with radius ranging from 10 cm to 100 km
  - Silica bodies, ice bodies, carbon bodies, C-type asteroids and S-type asteroids were simulated
    - Silica: SiO_2 with density of 2.00 g cm^{-3}
    - Ice: H_2O with density of 0.92 g cm^{-3}
    - Carbon: C with density of 2.00 g cm^{-3}
    - C-type: composition from K. Lodders and B. Fegley, 1998, density 2.23 g cm^{-3}
    - S-type: composition from K. Lodders and B. Fegley, 1998, density 3.80 g cm^{-3}
- $I_i(E_k)$: intensity of the *i*-th species of CRs impinging on the asteroid surface (mostly p, e^- and He nuclei)
- Two limiting CR spectra were assumed
  - Local Interstellar Spectra (LIS) from P. De La Torre Luque et al., 2021 - 2022
  - CR spectra at Earth (mainly AMS-02 measurements)
- Thus, the asteroid emission is bracketed between two limiting cases

Gamma-ray intensity from asteroids

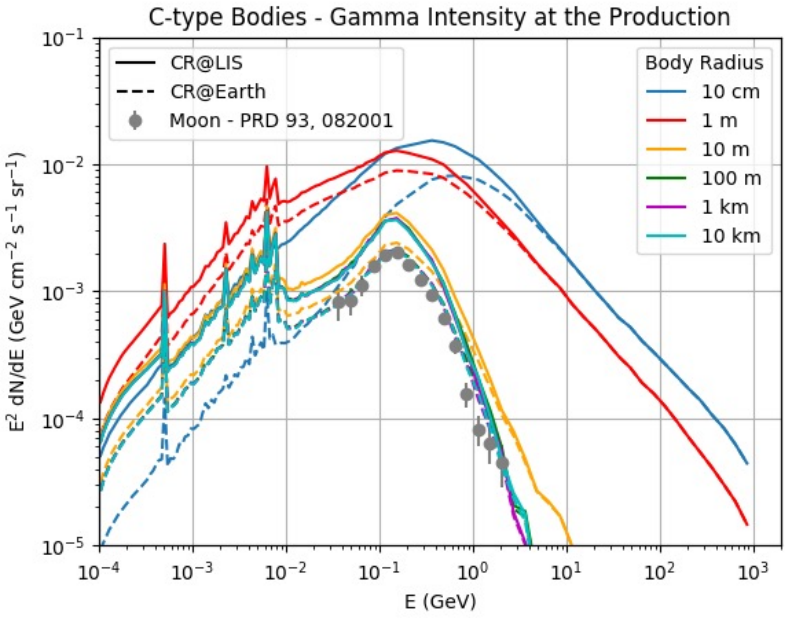

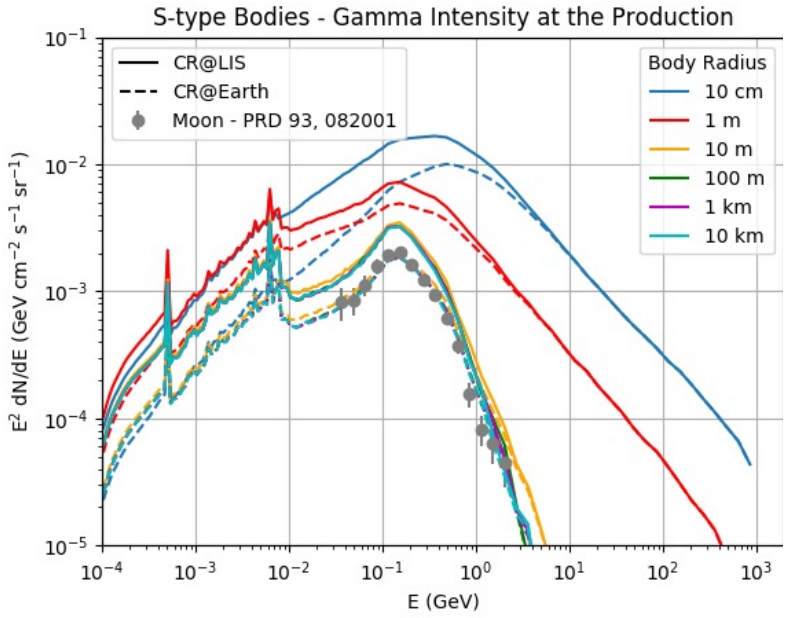

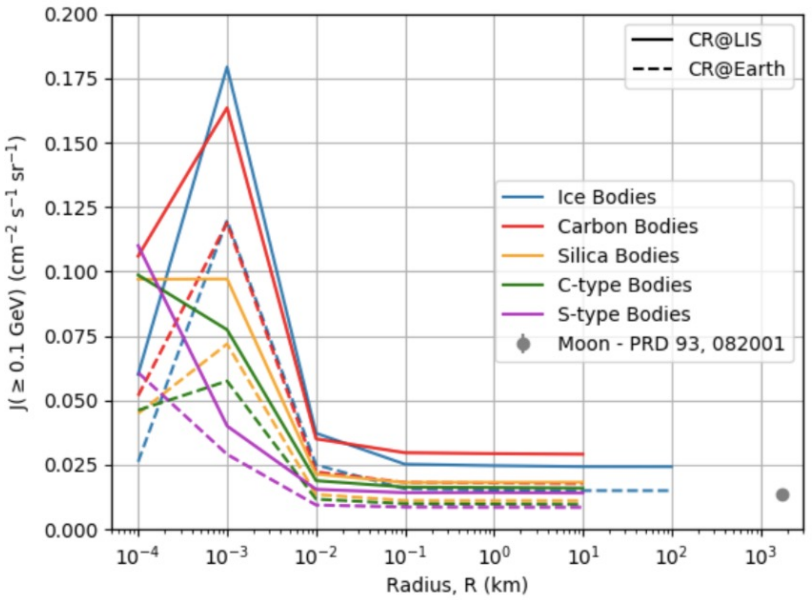

- Most lines in the spectra are due to photons emitted in nuclear de-excitation processes, while the line at 0.511 MeV is due to annihilations of positrons produced in the electromagnetic showers
- For asteroid size > 10 m, the shape does not change with the asteroid radius
  - CRs can penetrate down to depths of a few tens of g/cm^2
  - Gamma-ray absorption length is shorter
  - When the asteroid size > both these lengths, the gamma-ray production becomes independent of the size
  - The intensity of gamma rays from bodies of large size is close to the intensity of gamma rays emitted from the Moon measured by the *Fermi*-LAT (M. Ackermann et al., 2016)
    - For this reason, the Moon spectrum has been also used as a template for the asteroid spectrum (see next slides)
- For asteroid size < 1 m, the intensity at production decreases rapidly with decreasing radius
  - The asteroid size becomes $\lesssim$ typical interaction lengths in the simulated materials, which are of the order of tens of cm

Gamma-ray asteroid flux at the Earth

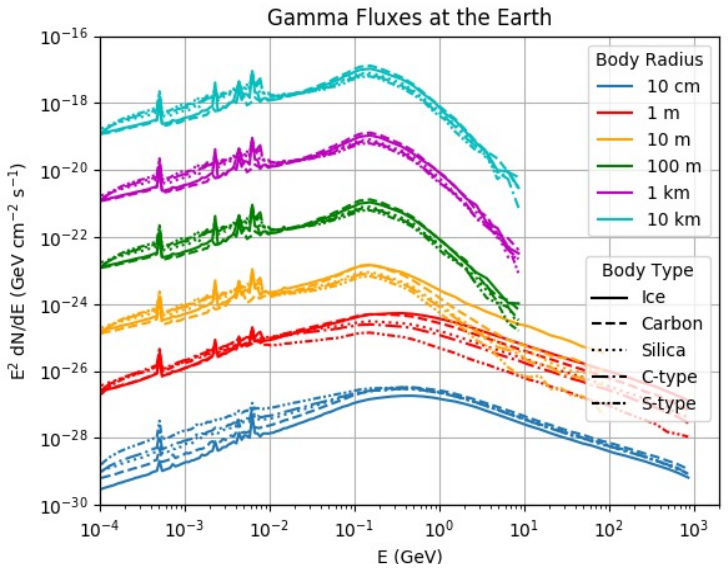

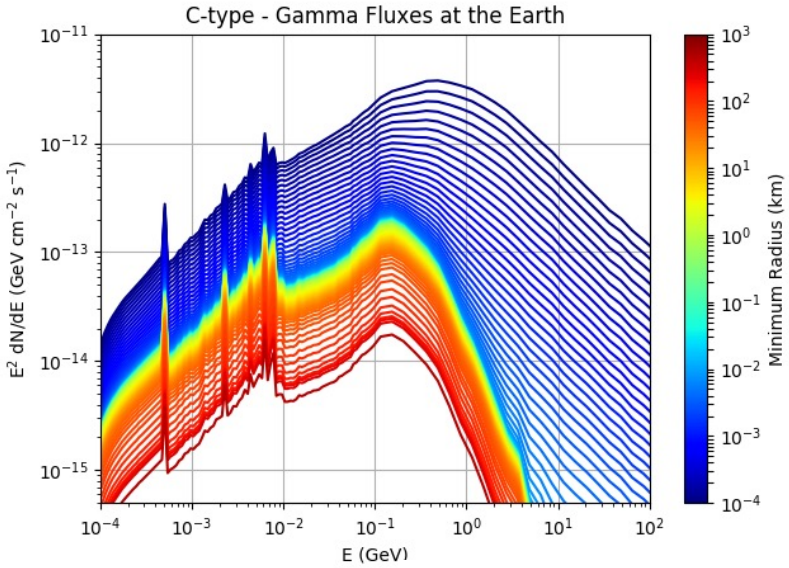

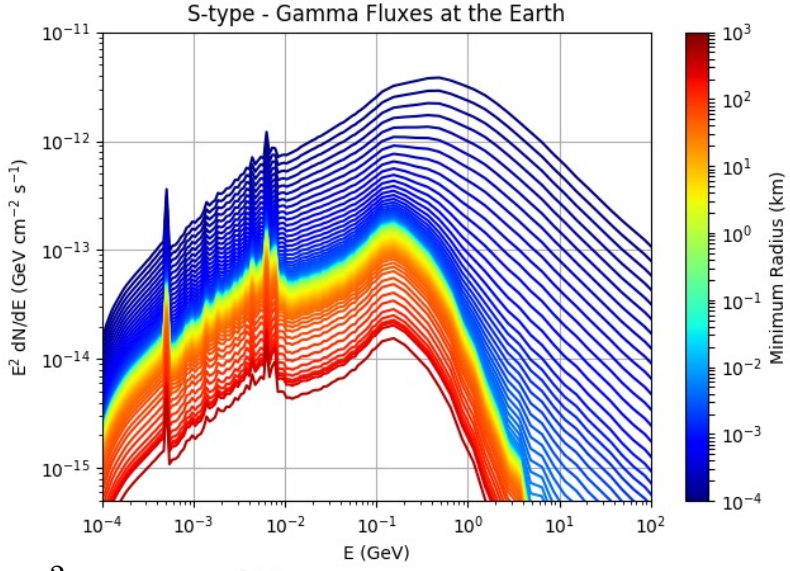

$$\phi_\gamma(E_\gamma, d, r) = \pi \frac{r^2}{d^2} I_\gamma(E_\gamma, r) N(r, d)$$

$$N(r, d) = 1, \qquad d = 2.7 \text{ AU}$$

$$\phi_\gamma(E_\gamma, d, r > r_0) = \int_{r_0}^{r_1} \frac{\pi r^2}{d^2} I_\gamma(E_\gamma, r) \frac{dN}{dr} dr$$

$$d = 2.7 \text{ AU}, \qquad r_0 \sim 10 \text{ cm}, \qquad r_1 \sim 500 \text{ km}$$

- The fluxes obtained with body radius $r > 10$ m have the same shape
- This is due to the effect for which the intensity of gamma rays emitted from the asteroids becomes independent of the size for large sizes
- Since the flux depends on the intensity and on a factor r^2, for $r > 10$ m the intensity contribution to the flux remains unchanged and the flux becomes dependent only on r^2

- dN/dr given by the model proposed at the beginning of the presentation: JPL catalog for $r > 1.25$ km, extrapolated Durda et al. model for $10 \text{ cm} < r < 1.25 \text{ km}$
- The gamma-ray emission at the site of production is almost independent of size for asteroid radii larger than a few tens of meters
- This is why, as r_0 increases, only the normalization of the curves changes, but the shape is almost the same

The *Fermi*-LAT experiment

- *Fermi* is a satellite observatory for photon energies from 8 keV up to the TeV region
- Its main instrument is the LAT (Large Area Telescope)
  - Based on $\gamma \rightarrow e^+ e^-$ conversion
  - It allows for a scan of the entire γ–ray sky every two orbits around the Earth
  - 16 tracker (TKR) modules, 16 calorimeter (CAL) modules and a segmented anti-coincidence detector (ACD)
- The TKR is composed of planes of silicon-strip detectors alternated with tungsten planes
  - It allows for reconstruction of the photon incidence direction
  - It is segmented into a *front* (thin converters) and a *back* section (thick converters)
- The CAL is composed of 96 CsI(Tl) crystals
  - It measures the energy of the shower produced by the incoming photon
- The ACD is composed of 89 plastic scintillator tiles
  - It is an anticoincidence shield which rejects charged cosmic rays

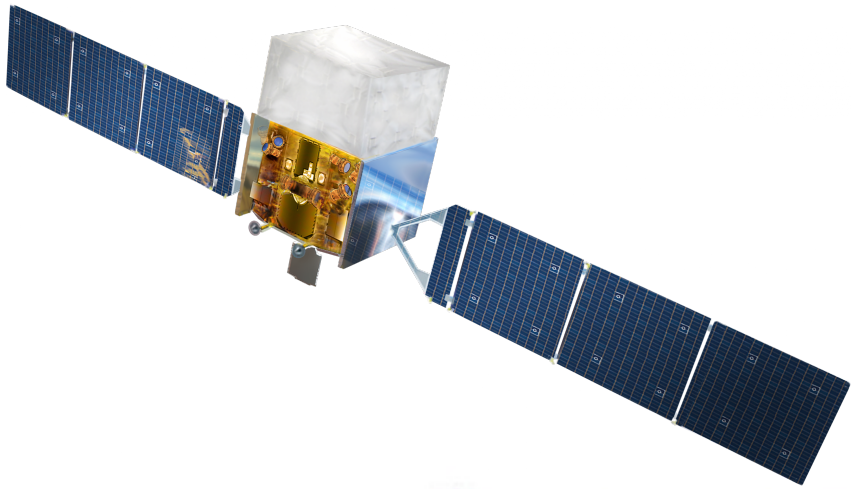

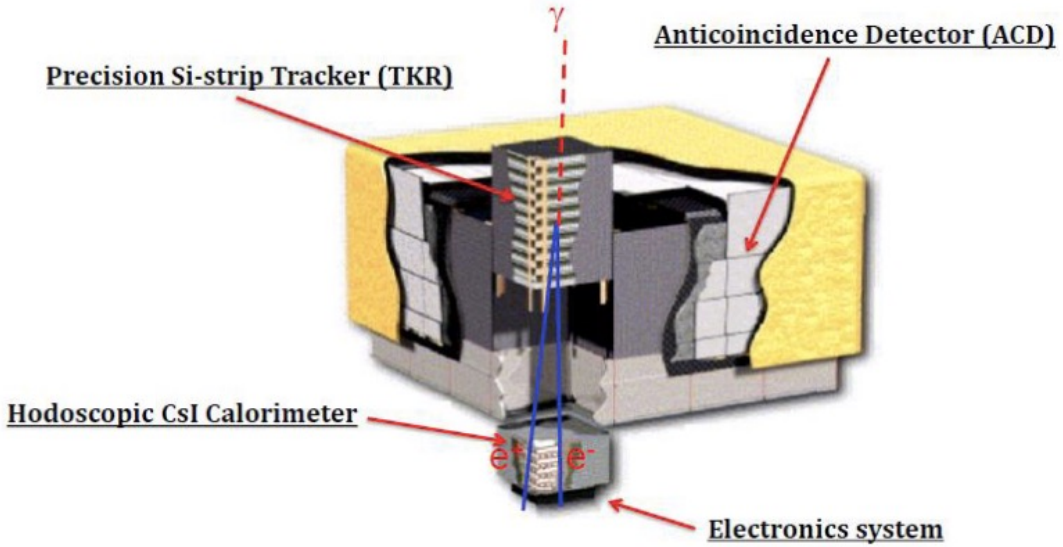

Fermi-LAT data analysis

- Since the beginning of the *Fermi* mission, four major data releases have been built, called *Passes*
  - The last major data release is called Pass 8
- Candidate photon events are divided into different classes, according to the purity of the data set
- A list of quantities, like arrival direction or energy, is associated to each photon event
- The statistical techniques adopted in the data analysis in this work are based on the maximization of the likelihood, built according to Poisson statistics, applied on the photon counts detected in the Region of Interest (RoI)
  - A *binned* likelihood analysis is performed, consisting in dividing the RoI at issue into spatial pixels and energy bins

$$\ln \mathcal{L} = \sum_{i,j} [n_{i,j} \ln \lambda_{i,j}(\alpha_k) - \lambda_{i,j}(\alpha_k)]$$

$n_{i,j}$, $\lambda_{i,j}$ = observed and expected counts in the pixel *i* and energy bin *j*
α_k = parameters to fit (describing, for example, the flux in the RoI)

- One can introduce the *test statistics*: $\mathrm{TS} = 2 \ln \left(\frac{\bar{\mathcal{L}}}{\bar{\mathcal{L}}_0} \right) = 2(\ln \bar{\mathcal{L}} - \ln \bar{\mathcal{L}}_0)$
- In this work, the TS value expresses the significance of a gamma-ray source: if TS ≥ 25, the significance of the source is ≥ 5σ, and one claims that the source has been detected
- If no detection is found, an upper limit can be set on the source flux
  - For example, a decrease in log-likelihood of 2.71/2 = 1.35 corresponds to a 95% C.L. upper limit

Fermi-LAT analysis of gamma rays from SSSBs

- Data selection:
  - Pass 8 P305 dataset
  - ULTRACLEANVETO event class (FRONT and BACK photons)
  - 149 months of data: Aug 2008 – Dec 2020
  - Energy between 56 MeV and 1.78 TeV, 8 bins/decade
  - Six RoIs along the ecliptic plane
    - 40° width in equatorial latitude and longitude
    - Minimum separation of ≃ 17° from the Galactic plane
- Selection of the Good Time Intervals (GTIs):
  - LAT operating in its standard science operation configuration
  - *Fermi* outside the South Atlantic Anomaly (SAA)
  - LAT z-axis at an angle < 70° with respect to the zenith
    - This prevents contamination from the Earth Limb
  - Minimum angular separation of 35° (45°) between Moon (Sun) direction and the center of each RoI
    - Each RoI is excluded from coverage for a few months of the year
- The analysis was performed using the *Fermi Science Tools* (version 2.0.8) and *fermipy* (version 1.0.1)
  - 1 analysis for each RoI, each year and each month
    - A possible signal from SSSBs should be time-dependent

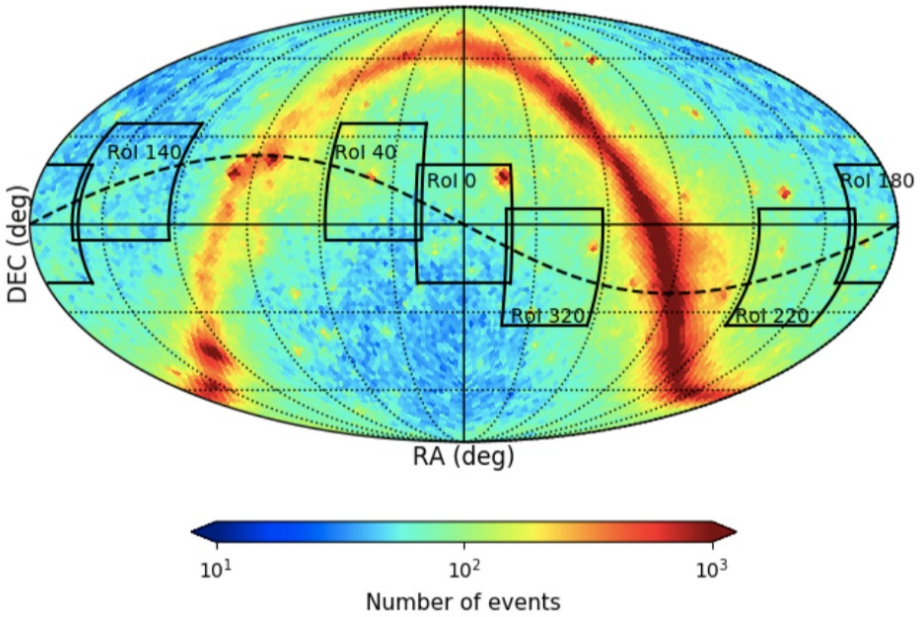

- Modeling of the gamma-ray emission and fit:
  - The point-like and extended sources in each RoI are taken from the 4th catalog of LAT sources 4FGL
  - The diffuse background templates (galactic and isotropic) developed by the *Fermi*-LAT collaboration are included
    - Only free normalization of sources within 25° w.r.t. the center of the RoI and with TS > 25
  - Asteroid diffuse model
    - Spectral model: power-law with index –2
    - Spatial model: the map defined in slide 4
    - Free parameter: normalization

Fermi-LAT analysis of gamma rays from SSSBs

Asteroid source model

Spectral model

$$\frac{dN_\gamma}{dE} = N_{0,\gamma}\left(\frac{E}{E_0}\right)^{-2}$$

Spatial model

$$\sum_i \frac{\omega(\lambda,\beta,d_i)}{\Delta\Omega\, d_i^2}$$

$E_0 = 100$ MeV, $N_{0,\gamma}$ in MeV^{-1} cm^{-2} s^{-1}

- In all fits, TS ≈ 0 (asteroid source not significantly detected in any RoI and time interval)
- In each fit, derived the UL on the asteroid flux above 56 MeV at 95% CL: peaked at $\simeq 2 \times 10^{-6}$ cm^{-2} s^{-1}
- The normalization of the galactic and isotropic components are close to 1 and appear to be anticorrelated

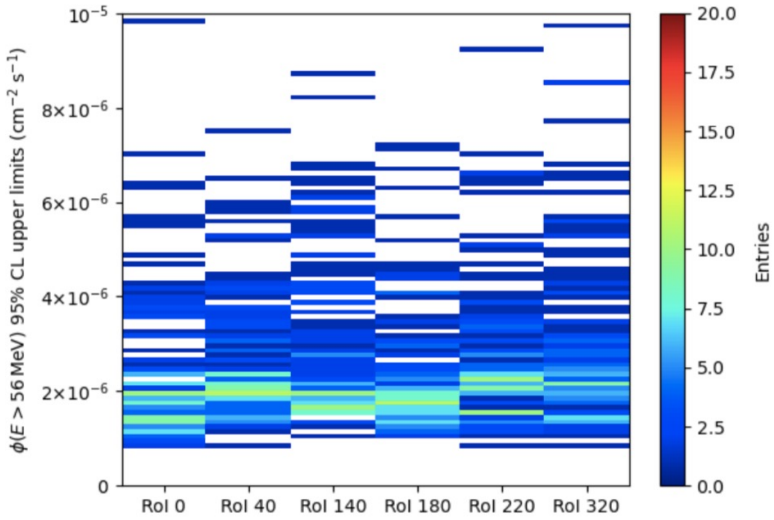

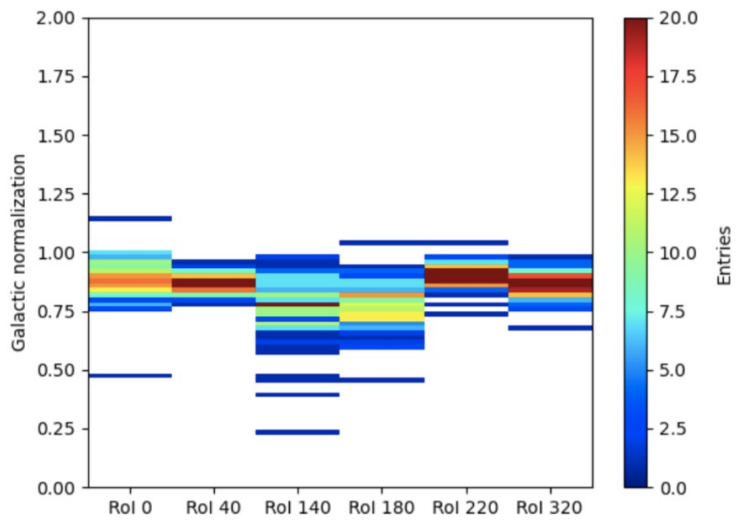

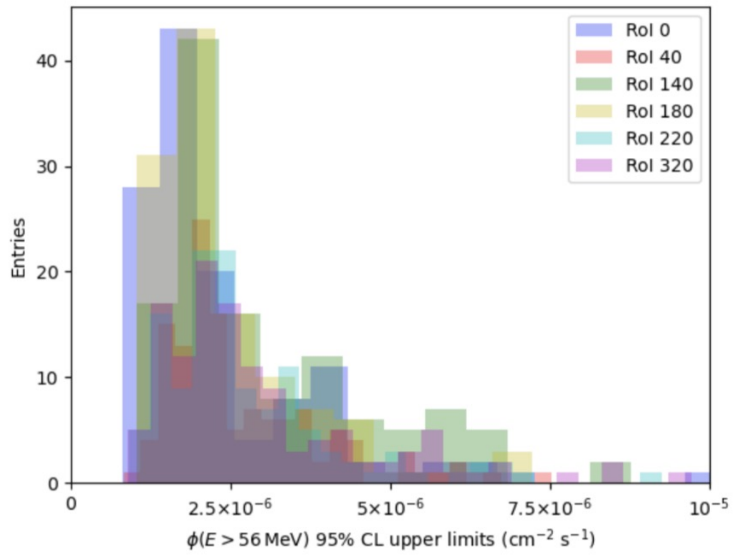

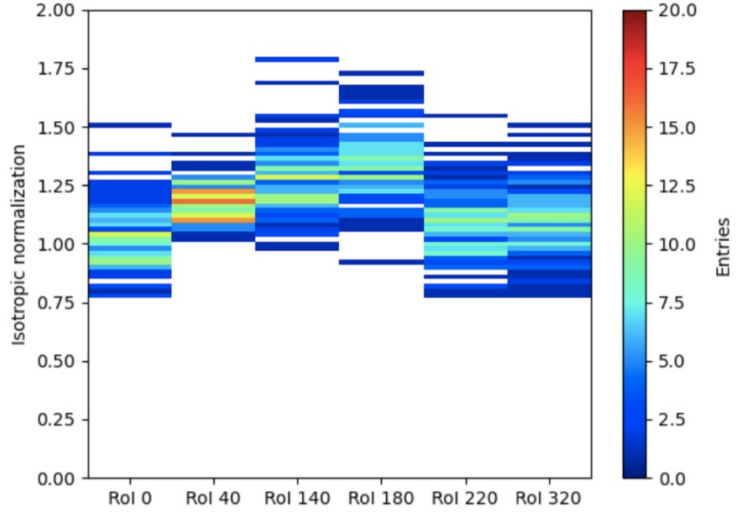

Combined likelihood analysis

- In each energy bin, the likelihood profile for the flux from asteroids was evaluated
  - Parameter $N_{0,\gamma}$ varied, spectral index kept fixed to 2
- All profiles in each energy bin, RoI and time window were combined
  - To evaluate constraints on a possible source population with spectral shape $f(E)$ and free norm. C

$$\ln \mathcal{L}(C) = \sum_s \sum_i \ln \mathcal{L}_i^s(C)$$

- $\mathrm{TS} = -2\left[\ln \mathcal{L}(C=0) - \ln \mathcal{L}(C_{max})\right]$
- The 95% CL UL is the value of C for which

$$\ln \mathcal{L}(C) = \ln \mathcal{L}(C_{max}) - 2.71/2$$

- More powerful approach in the search of a possible tiny gamma-ray signal from a population of identical sources

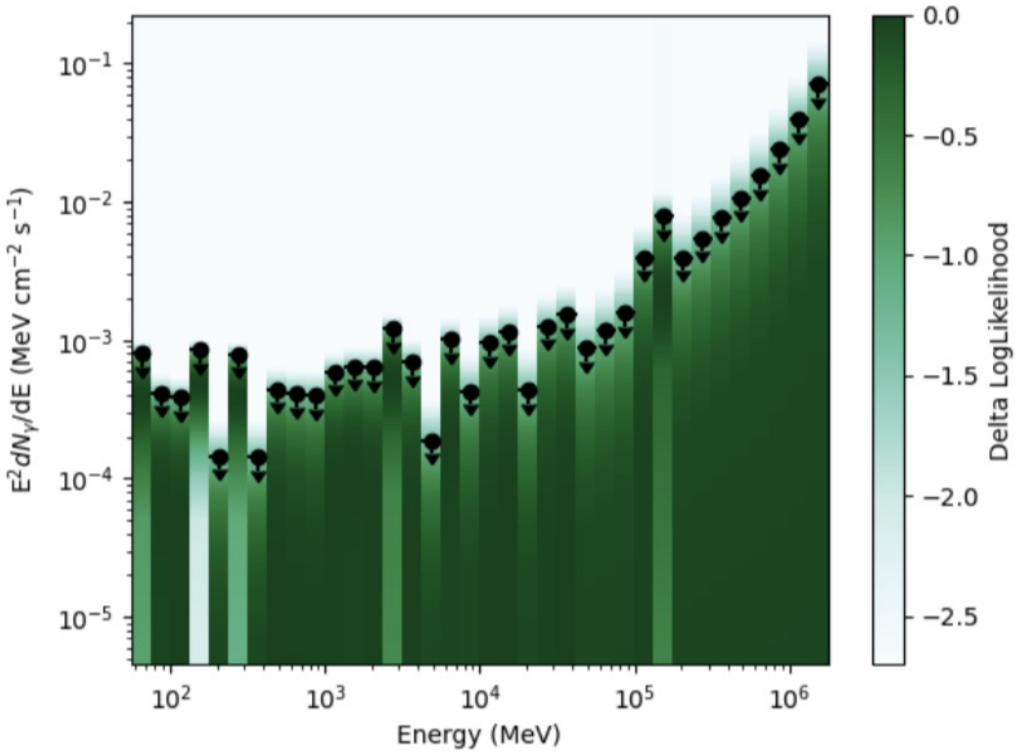

Combined likelihood analysis

- This approach was used to set ULs on the asteroid model assumed in the previous section
  - In this case, $f(E) = (E/E_0)^{-2}$
- First, the likelihood profiles for individual RoIs in all time intervals were combined
  - In all RoIs, TS < 0.014
  - Asteroid source described by the aforesaid model not significantly detected
- Then, the likelihood profiles for all RoIs and all time intervals were combined, providing a global TS of 0.043, still under the detection threshold
- The ULs obtained combining all the time intervals in an individual RoI are a factor 10 stronger than those obtained in the analysis of the same RoI in an individual time interval
- A further improvement of about a factor 10 is obtained combining the data from all RoIs and all time intervals

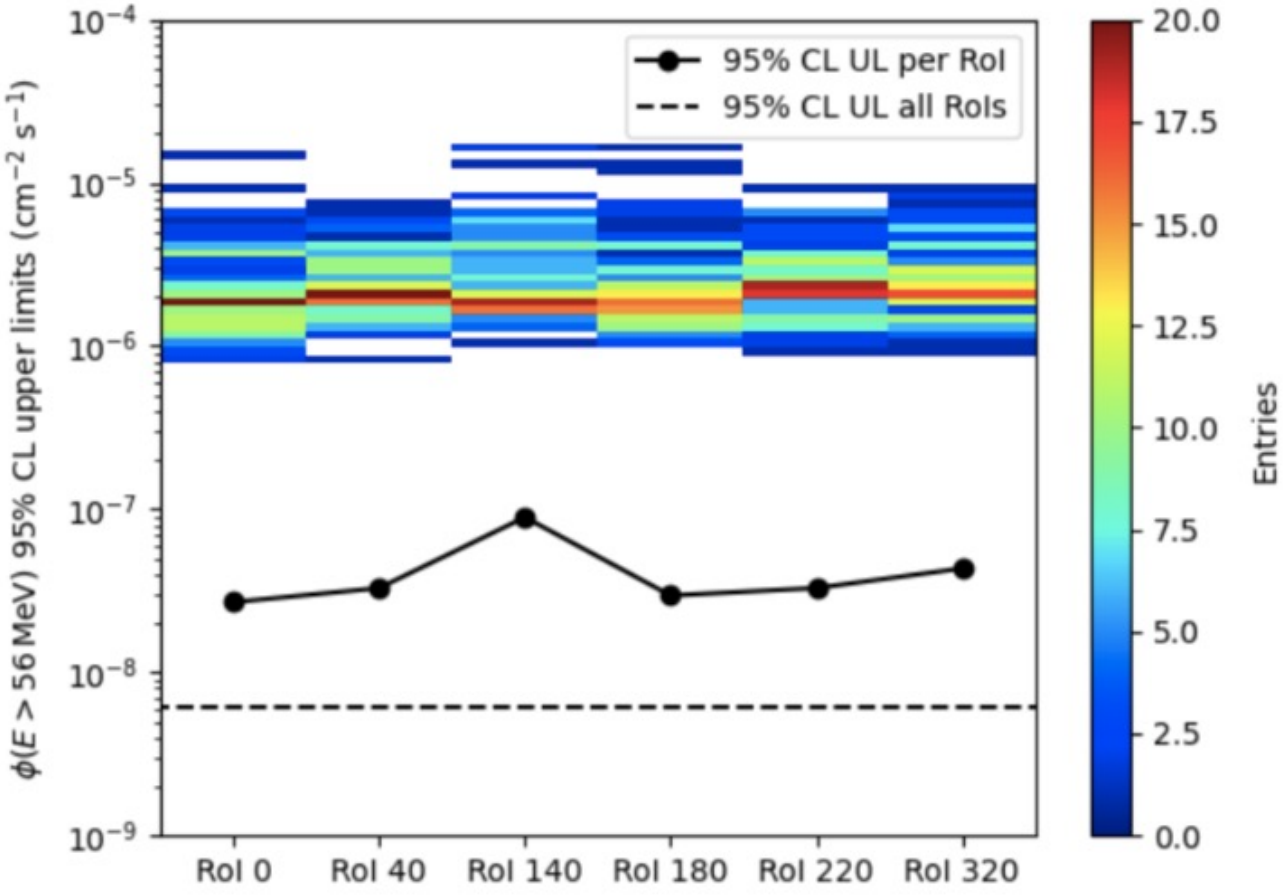

Population model-independent analysis: constraints on $N_{tot}(r)$

- The combined analysis procedure was implemented using for the asteroid source the spectral intensity shape model $f(E) = I_\gamma(E, r)$ with fixed value of the asteroid radius
- This approach allows for setting constraints on $N_{tot}(r)$ (total number of asteroids with radius r) for each value of the radius r
- The upper limit on $N_{tot}(r)$ was calculated assuming that all asteroids have the same radius and composition
- The signal from the asteroids was found to be not significant, hence the constraints on the normalization constant C were evaluated
- The UL at 95% CL on the gamma-ray flux, expressed as $\bar{C}\, I_\gamma(E, r)$, can be converted into an upper limit on $N_{tot}(r)$, from the following equation:

$$\phi_\gamma(E_\gamma, r, \lambda, \beta) = \pi r^2 I_\gamma(E_\gamma, r) N_{tot}(r) \sum_{i \in l.o.s.} \frac{w(\lambda, \beta, d_i)}{\Delta\Omega\, d_i^2}$$

integrated over the whole sky: $\phi_{\gamma,\mathrm{UL}}(E, r) = \bar{C} I_\gamma(E, r) = \mathcal{B}\pi r^2 I_\gamma(E, r) N_{\mathrm{UL}}(r)$

$$\Longrightarrow N_{\mathrm{UL}}(r) = \frac{\bar{C}}{\mathcal{B}\pi r^2}$$

Population model-independent analysis: constraints on $N_{tot}(r)$

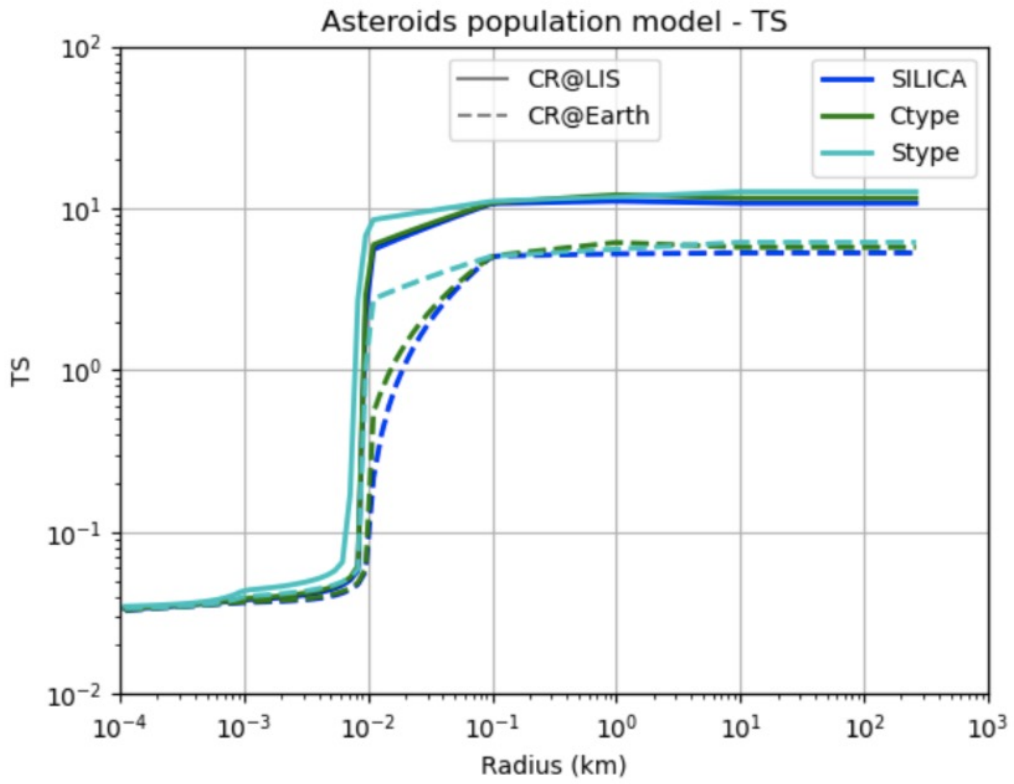

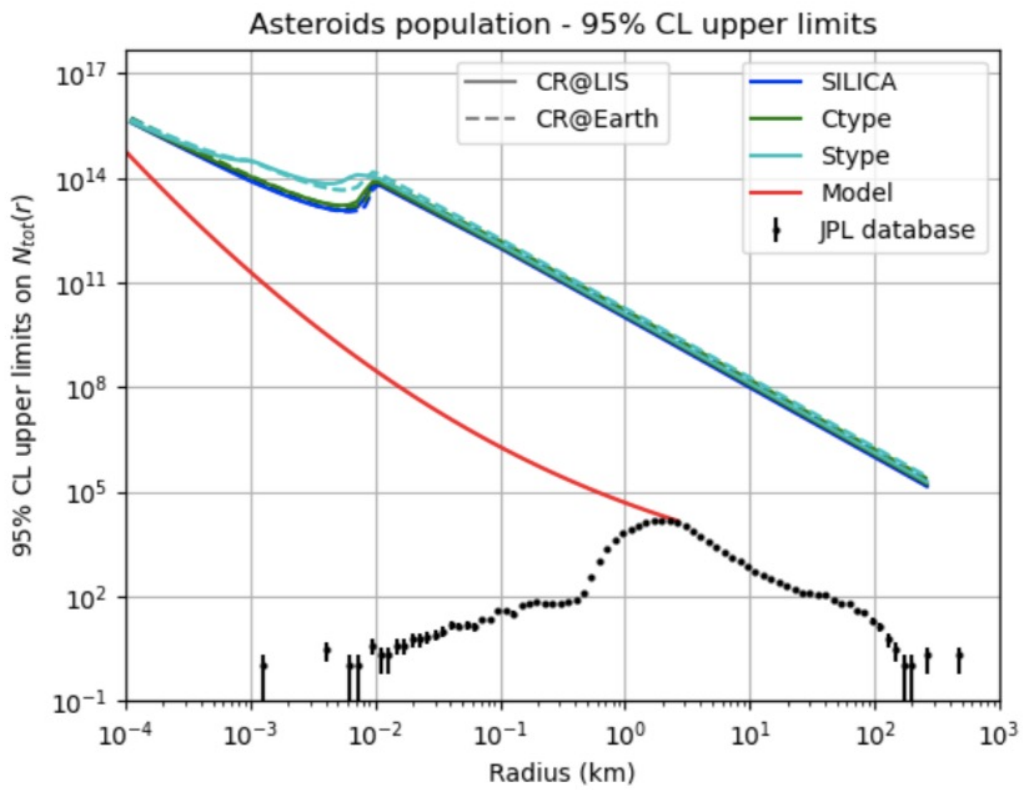

- For $r > 10$ m, the TS is almost constant, since the gamma-ray intensity becomes independent of r
- For smaller r, the spectral shape of the gamma-ray intensity is harder, and it is more disfavored by the data, resulting in a TS closer to zero
- Since the TS does not exceed the value of ~ 10, the asteroid source is not significantly detected for any value of r
- The constraints obtained with the different classes of asteroids are similar for radii below 10 m and above 100 m
- ULs LIS vary between 4×10^{15} and 1.4×10^{5}, ULs Earth between 5.2×10^{15} and 2.0×10^{5} from $r \simeq 10^{-4}$ km to 300 km

Model-dependent analysis: constraints on $N_{tot}(r \geq r_{min})$

- The combined likelihood analysis was used to set a constraint on the asteroids population model proposed in slide 3
  - It follows the JPL catalog for $r > 1.25$ km, the extrapolated Durda et al. model for $10\ \mathrm{cm} < r < 1.25\ \mathrm{km}$
- Cumulative flux of asteroids: $\phi_{\gamma,c}(E) = \mathcal{B} \sum_{r=r_{min}}^{r_f} \pi r^2 I_\gamma(E,r) N_{tot}(r)$ $\quad r_f \simeq 300$ km
- For a given value of r_{min}, this is $f(E)$; the ULs on C are then converted into ULs on the cumulative population model

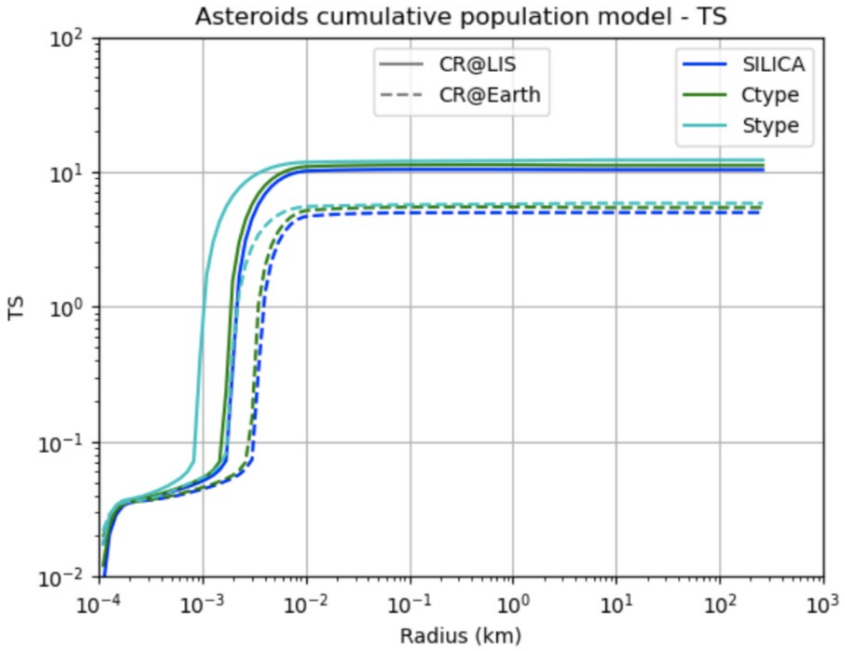

- TS $\simeq$ 0 for $r_{min} < 10^{-3}$ km
- TS increases for larger values of r_{min}, due to the change of shape of I_γ
- TS reaches a limiting value of ~10, not significant

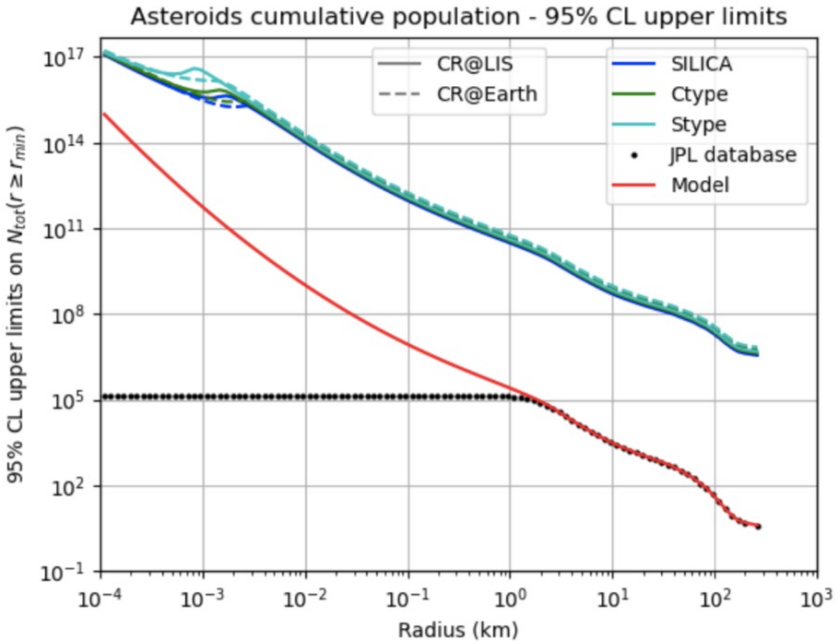

- The ratio between the ULs and the population predicted by the model increases with r_{min} (from 10^2 to 10^6)

Comparison between asteroids and Moon flux

- As a spectral model $f(E)$, the Moon flux measured by the LAT in its first 7 years was used
- The 95% CL UL on the asteroid flux is 0.39 times the Moon flux
- The plot shows the ratio between asteroids and Moon flux, assuming:
  - Asteroid size distribution described by a PL of index α
  - Asteroids made of silica with density 2 g/cm^3 and $d = 2.7$ AU
  - Asteroid intensity = Moon intensity (true for large radii, see slide 10)

$$\frac{\phi}{\phi_{\leftmoon}} = \begin{cases} a \dfrac{1}{R_{\leftmoon}^2} \dfrac{D_{\leftmoon}^2}{d^2} \times \dfrac{r_1^{3-\alpha} - r_0^{3-\alpha}}{3-\alpha} & \text{for } \alpha \neq 3 \\ a \dfrac{1}{R_{\leftmoon}^2} \dfrac{D_{\leftmoon}^2}{d^2} \times \log \dfrac{r_1}{r_0} & \text{for } \alpha = 3 \end{cases} \qquad a = \begin{cases} \dfrac{3M}{4\pi\rho} \times \dfrac{4-\alpha}{r_1^{4-\alpha} - r_0^{4-\alpha}} & \text{for } \alpha \neq 4 \\ \dfrac{3M}{4\pi\rho} \times \dfrac{1}{\log \frac{r_1}{r_0}} & \text{for } \alpha = 4 \end{cases}$$

$r_0 = 10^{-4}$ km, $r_1 = 470$ km

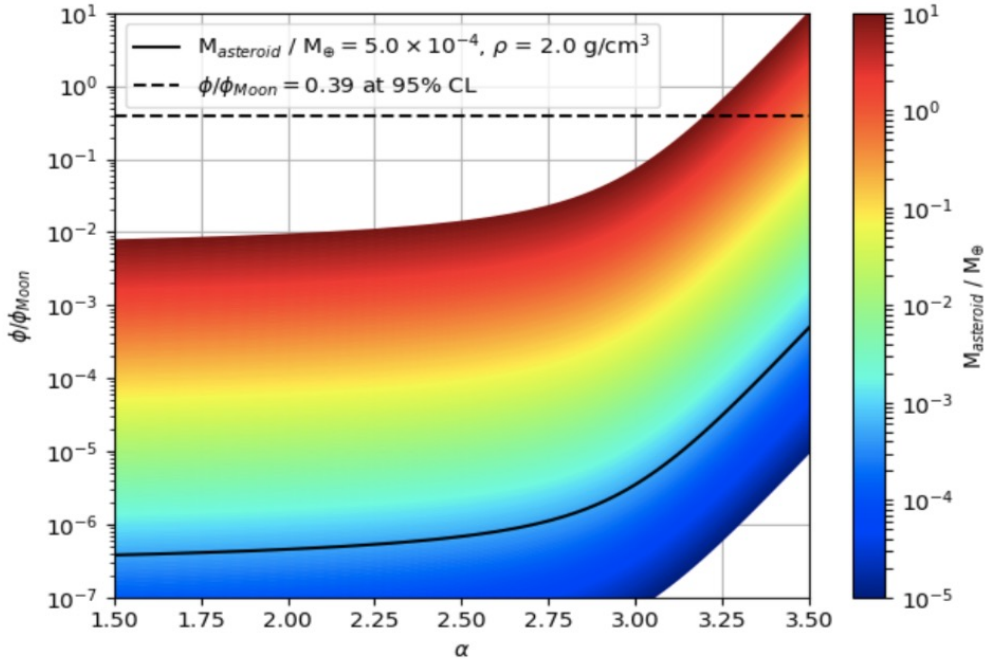

- At 95% CL, all values of α and asteroid total masses above the dashed threshold can be ruled out when modelling the asteroids flux as in the previous equation

Conclusions

- In this work, a 12-year LAT data sample has been used to study the gamma rays from the ecliptic plane
  - Constraining gamma-ray emission from SSSBs
  - Constraining population of SSSBs with $r < 1$ m
  - Testing different size distribution models
- In this analysis, the asteroid emission has been modeled with a spatial and a spectral template
  - Free parameter: normalization
  - The TS was computed and it was found that the asteroids source was not detected
- A combined likelihood analysis has been also implemented
  - More powerful approach in the search of a possible tiny gamma-ray signal from a population of identical sources
  - Used to constrain the asteroids population
  - The TS of the possible asteroid source is $\lesssim 10$ for asteroids of any radius r: not sufficient for claiming a detection
  - ULs at 95% CL vary between 10^{15} for $r \simeq 10^{-4}$ km and 10^{5} for $r \simeq 300$ km
  - Constraining the cumulative size model previously described: TS $\lesssim 10$ for any radius, ULs at 95% CL about 100 times the model for $r \simeq 10^{-4}$ km
  - It is possible to use this procedure with different models: the ULs will depend on the chosen model
- Combined likelihood analysis repeated assuming the asteroids flux to be given by the Moon flux measured in the first 7 years of LAT operation
  - UL at 95% CL of 0.39 for the ratio between asteroids and Moon fluxes
  - If SSSBs size distribution = PL of index α, this UL provides a threshold to the values that the asteroid total mass and α can assume
- Analysis techniques and results published in ***The Astrophysical Journal*, 951(1):13, June 2023**

BACK-UP SLIDES

Durda et al. model

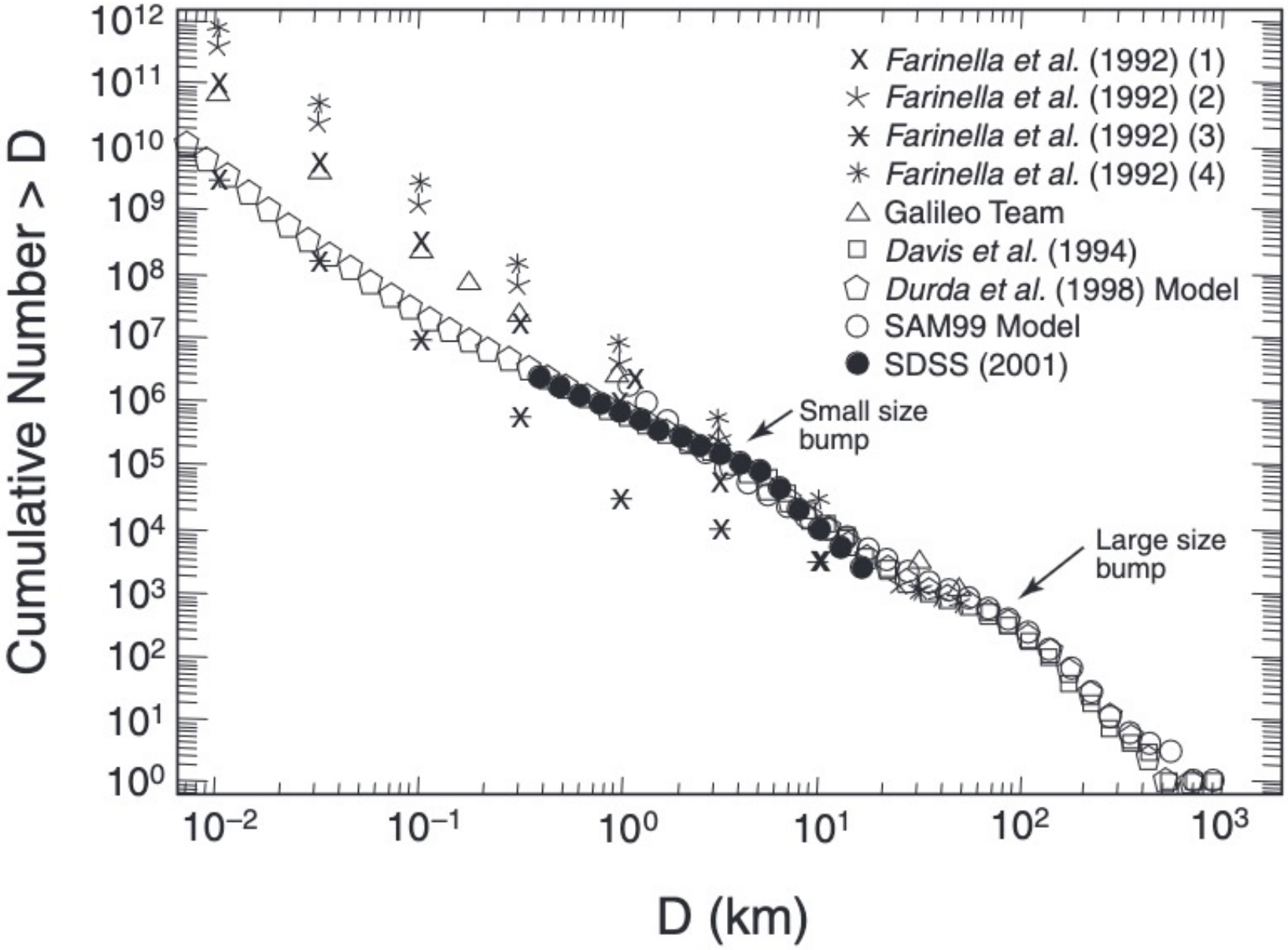

Davis et al. (2002)

Asteroid orbital parameters

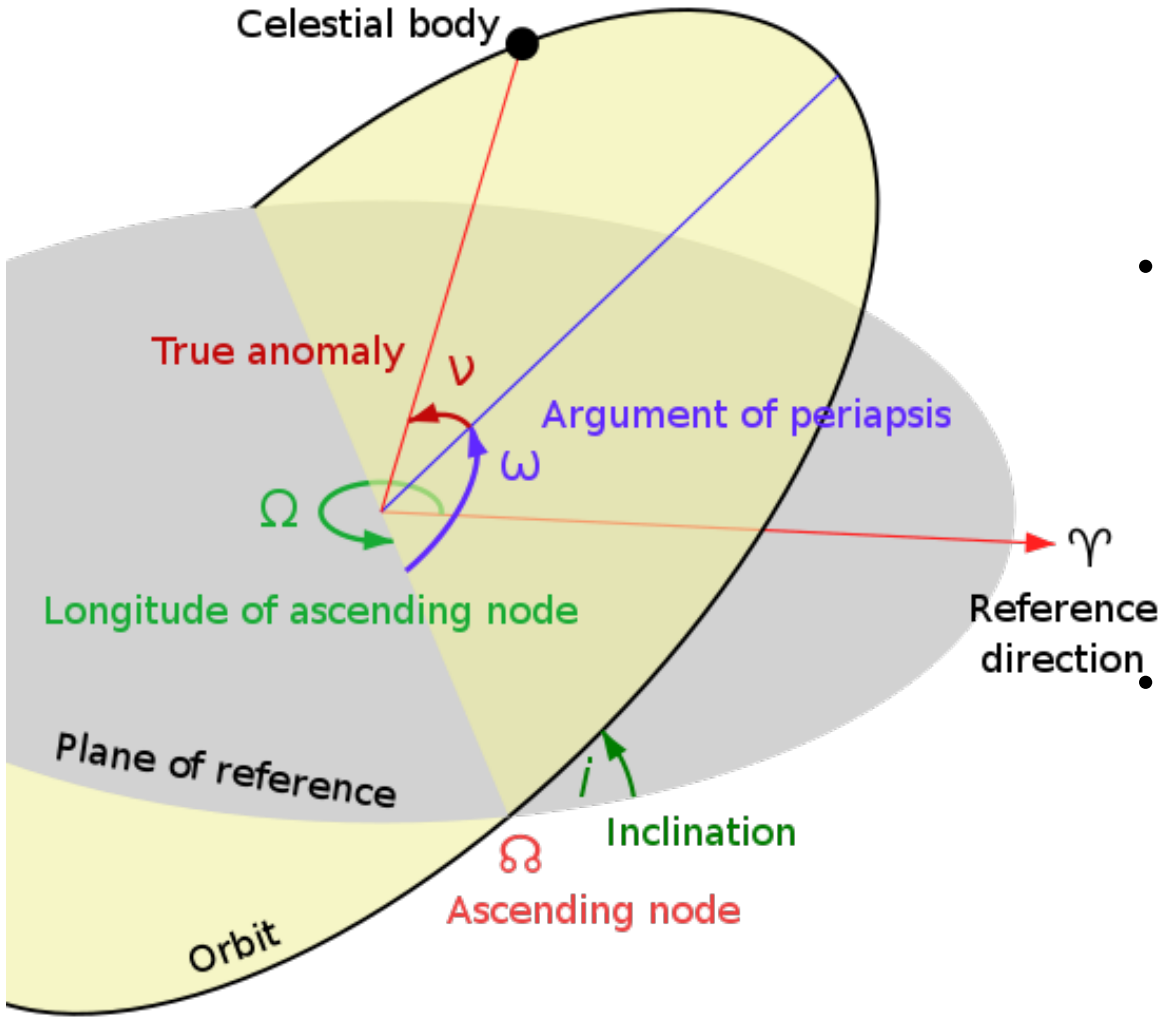

- An asteroid orbit is characterized by four parameters:
  - orbit major semiaxis l
  - inclination angle i of the orbit with respect to the ecliptic plane
  - longitude Ω of the ascending node
  - the argument of periapsis ω
- The asteroid position on the orbit is given by the «true-anomaly» angle ν

Wikipedia 2022

Distributions and correlations between orbital parameters

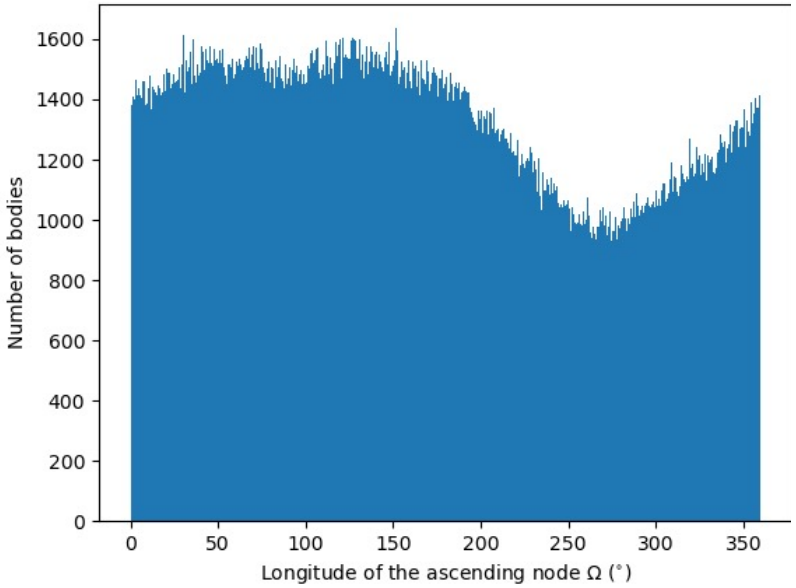

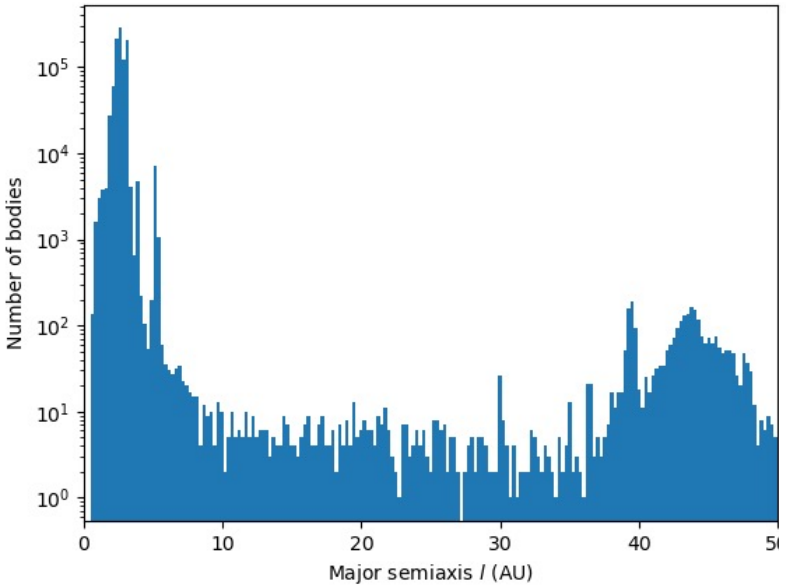

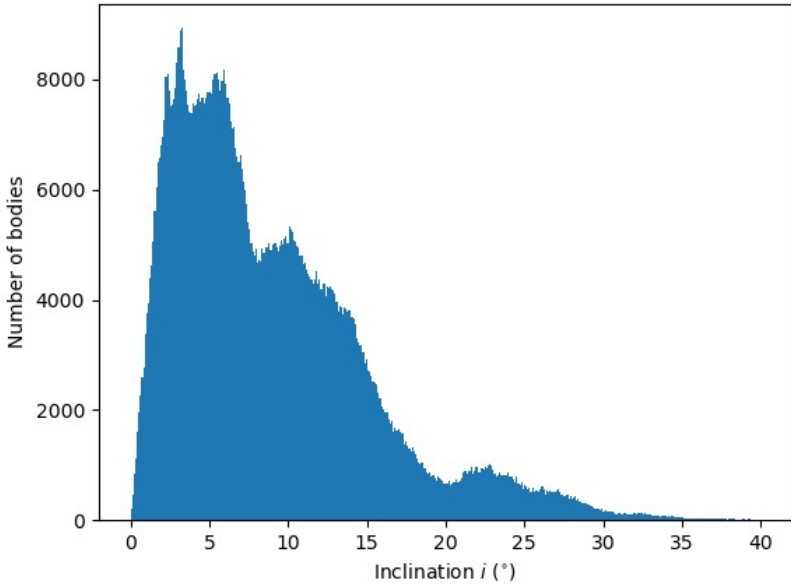

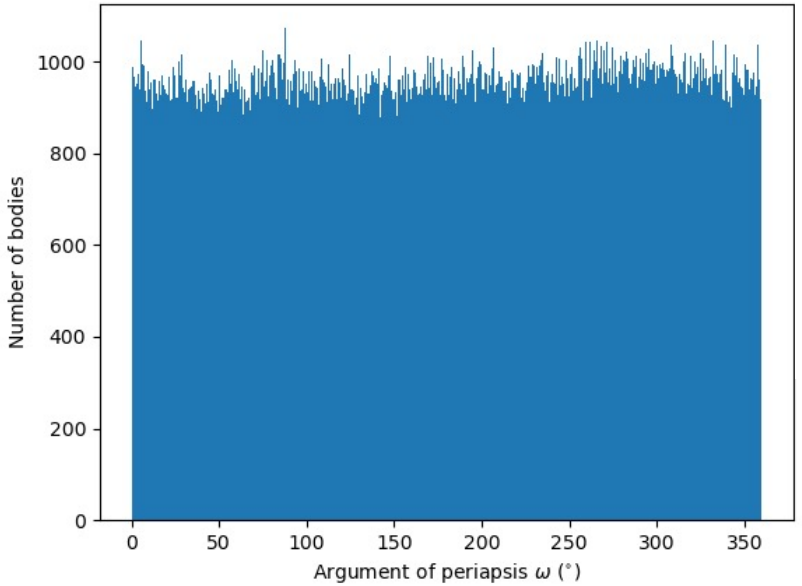

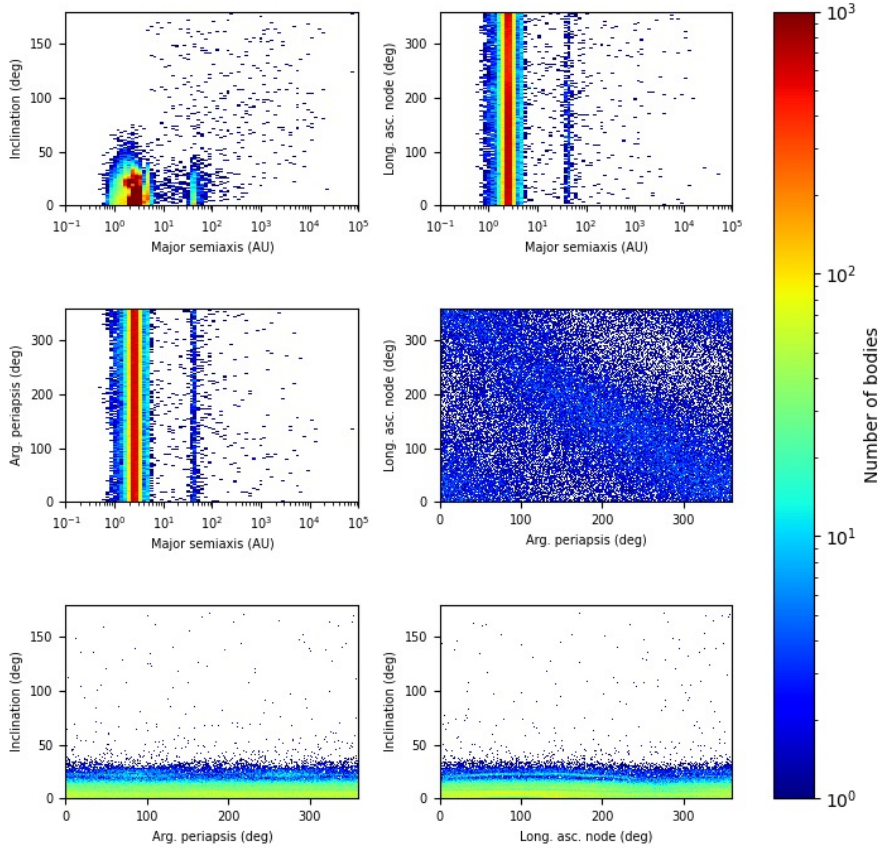

Jet Propulsion Laboratory, Small-Body Database, 2022

Average asteroid distance from the Earth as a function of its position in the sky

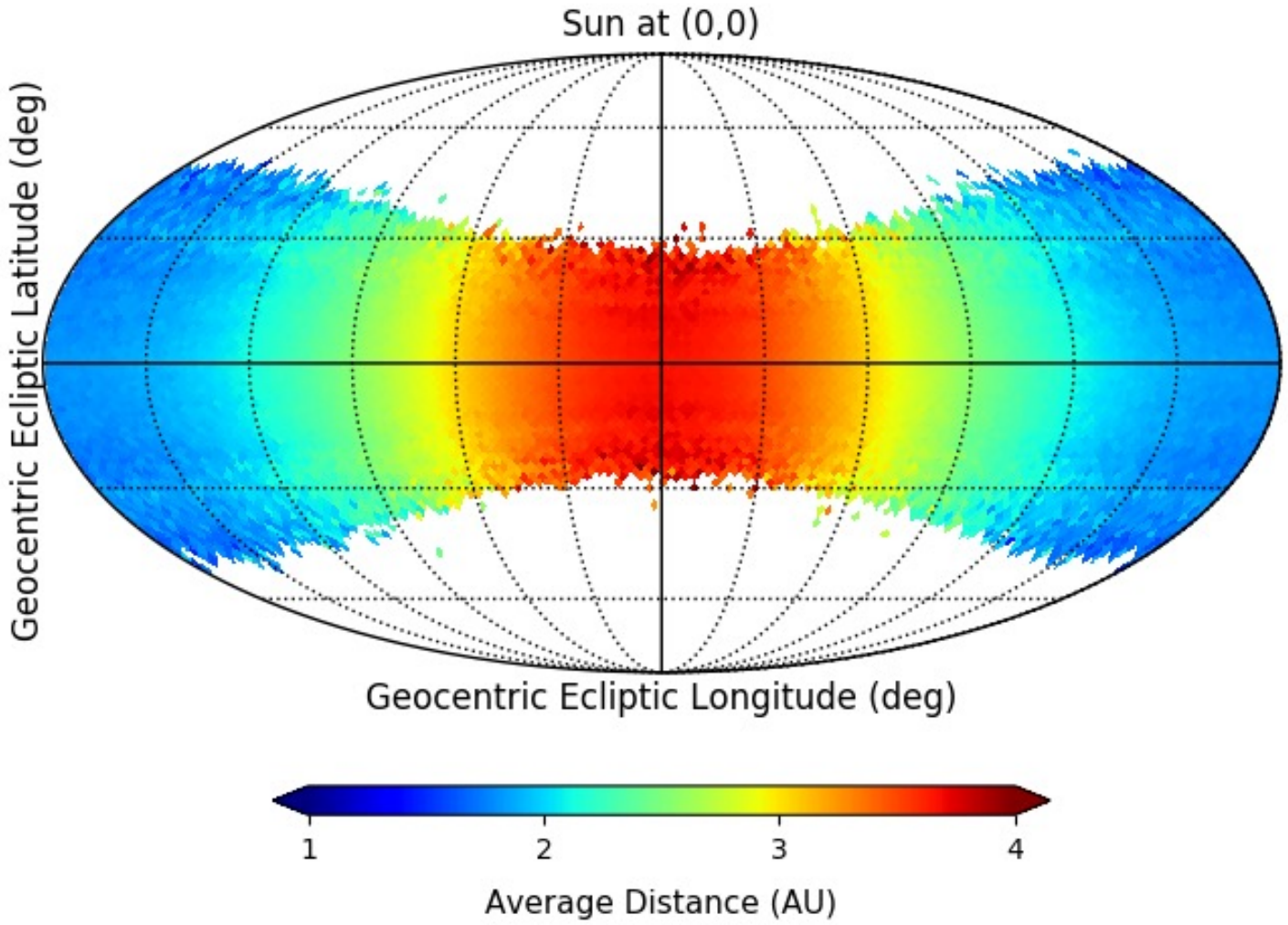

Solar modulation

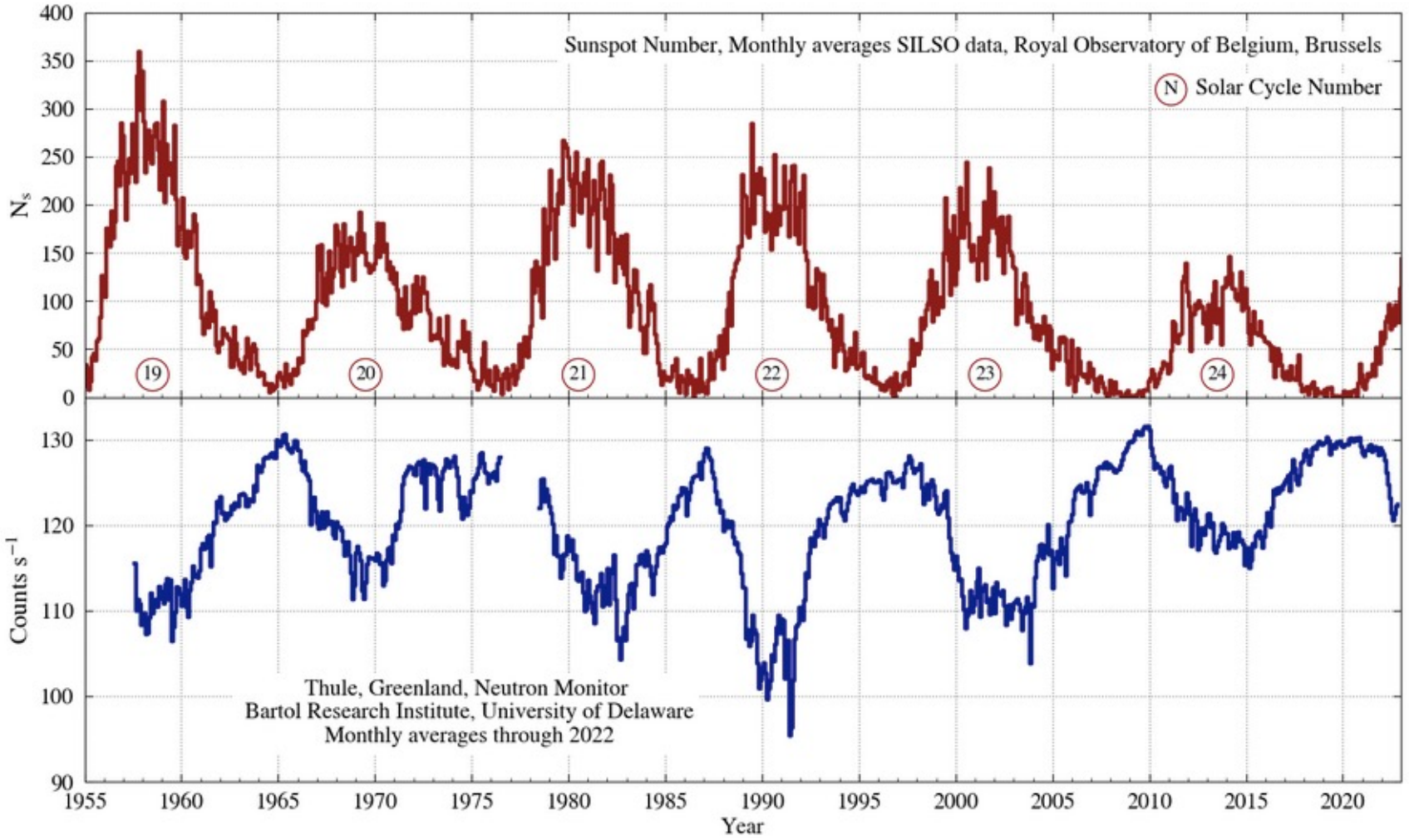

University of Delaware and Bartol Research Institute. Neutron Monitor Program
https://neutronm.bartol.udel.edu/

Spectrum of CRs

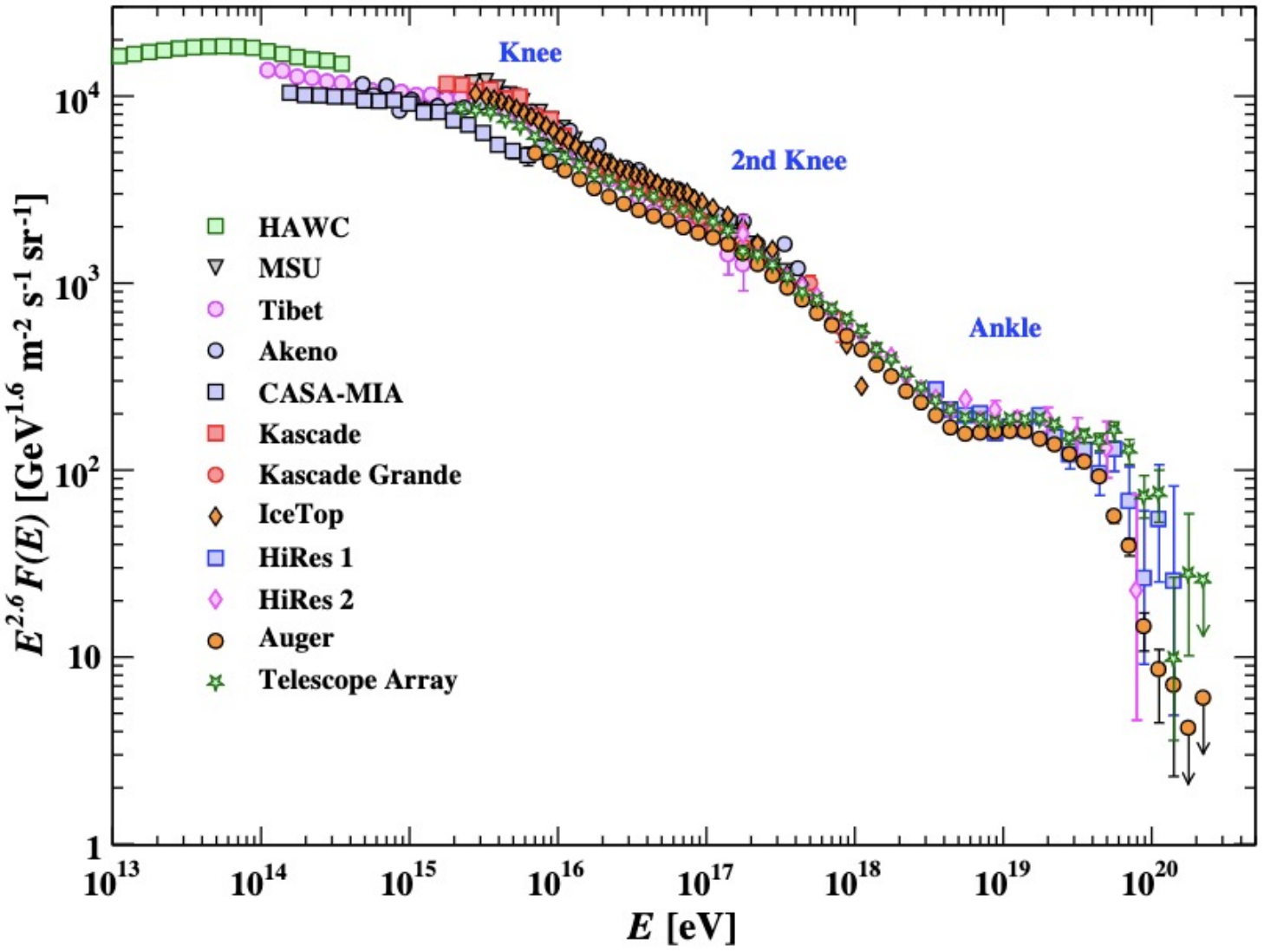

CR flux as a function of the energy per nucleus, measured by air-shower experiments

R. L. Workman et al., 2022

Spectrum of CRs

- For $E > 1\mathrm{GeV}$, up to a hundred EeV, the CR spectrum can be described by a power-law with index depending on the energy range:

$$F(E) \approx 1.8 \times 10^4 (E/1\,\mathrm{GeV})^{-\alpha} \frac{\mathrm{nucleons}}{\mathrm{m^2\,s\,sr\,GeV}}$$

  - $\alpha \simeq 2.7$ for $E < 10^{15}\mathrm{eV}$ (*knee* at $10^{15}\mathrm{eV}$)
  - $\alpha \simeq 3$ for $10^{15}\mathrm{eV} < E < 3 \times 10^{18}\mathrm{eV}$ (*ankle* at $10^{18}\mathrm{eV}$)
  - $\alpha \simeq 2.7$ for $3 \times 10^{18}\mathrm{eV} < E < 10^{19}\mathrm{eV}$ (GZK cut-off)

- 98% of CRs are made of protons and nuclei
  - 87% protons, 12% helium, 1% heavier nuclei

- 2% of CRs are made of electrons

Spectrum of CRs

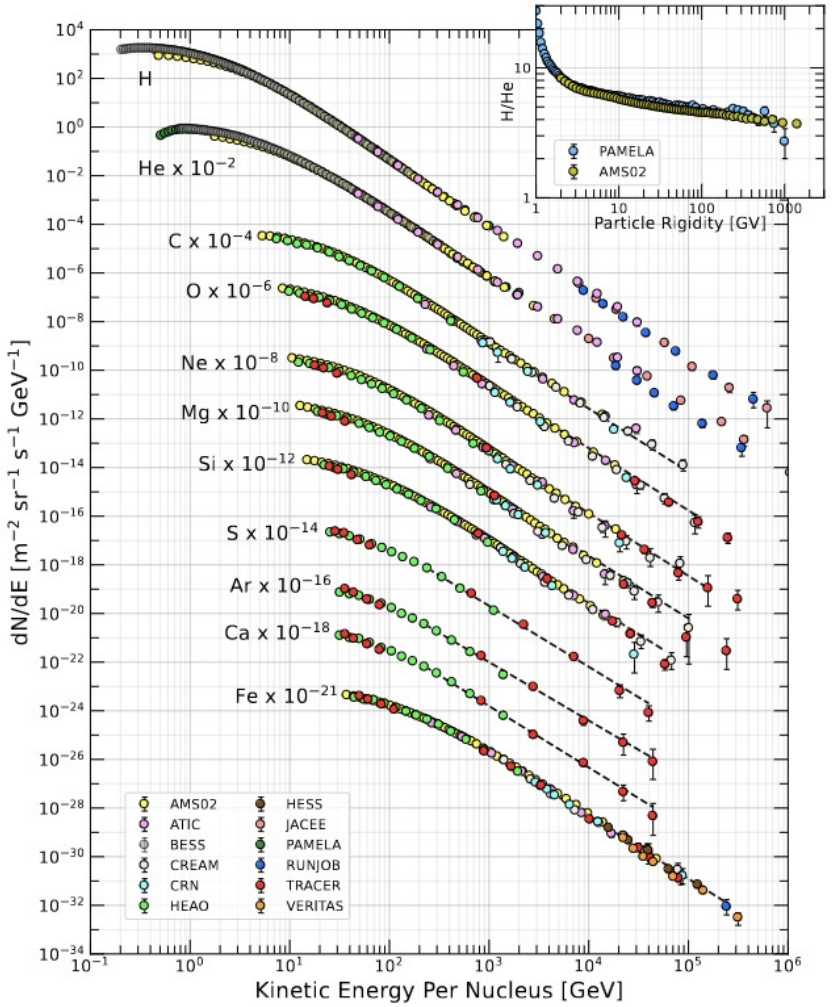

Flux for each CR component
R. L. Workman et al., 2022

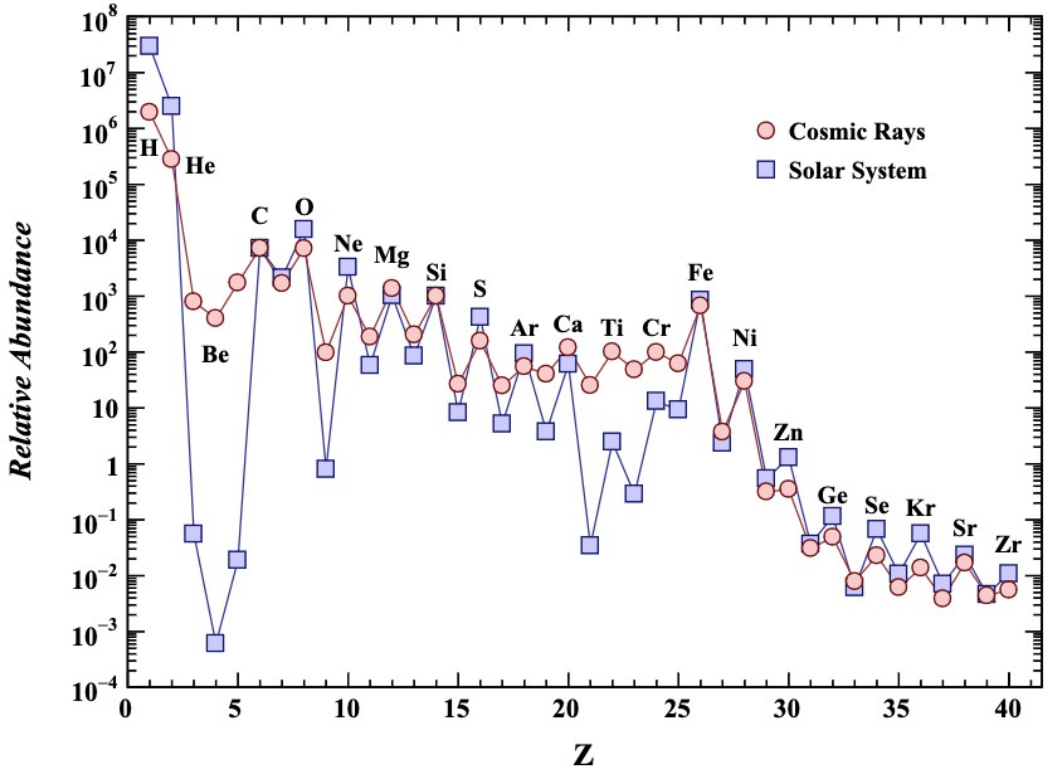

Chemical abundances in CRs and in the Solar System
R. L. Workman et al., 2022

Spectrum of CRs

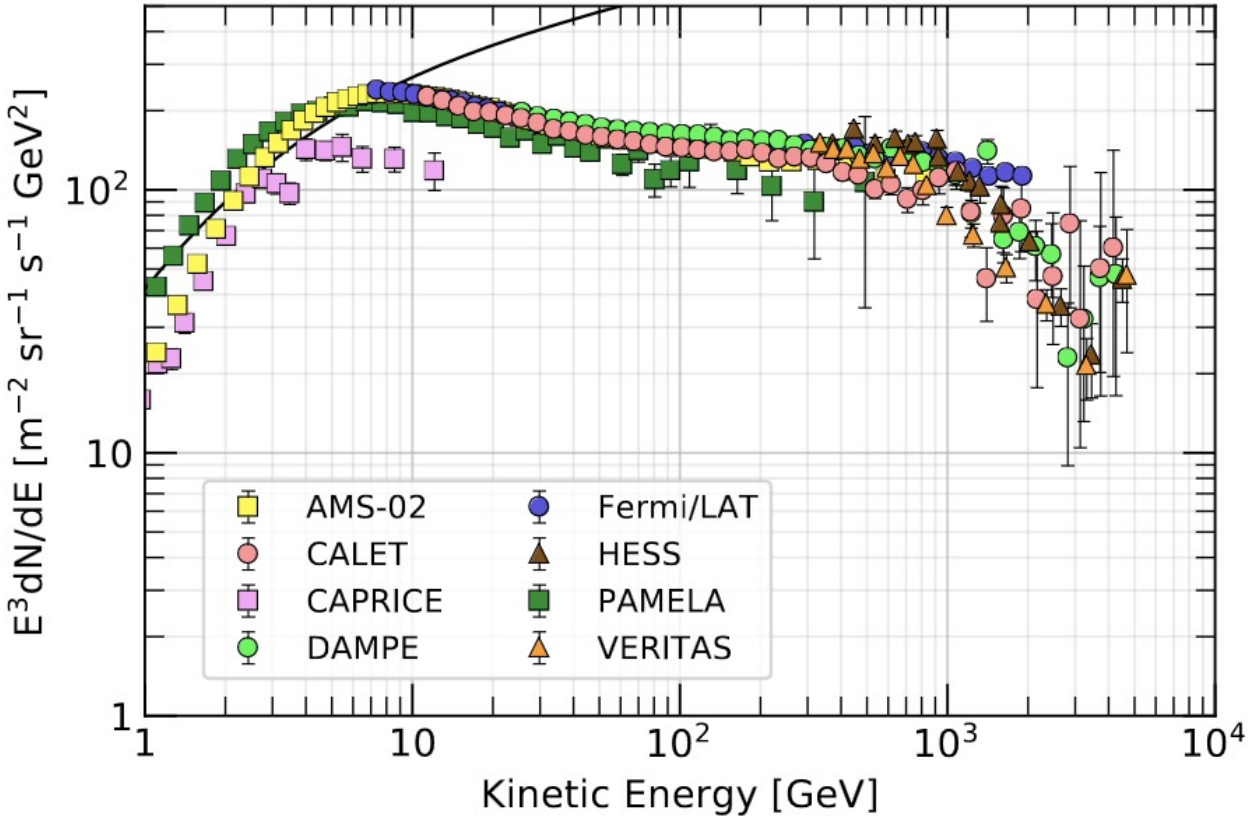

Electron plus positron spectrum
R. L. Workman et al., 2022

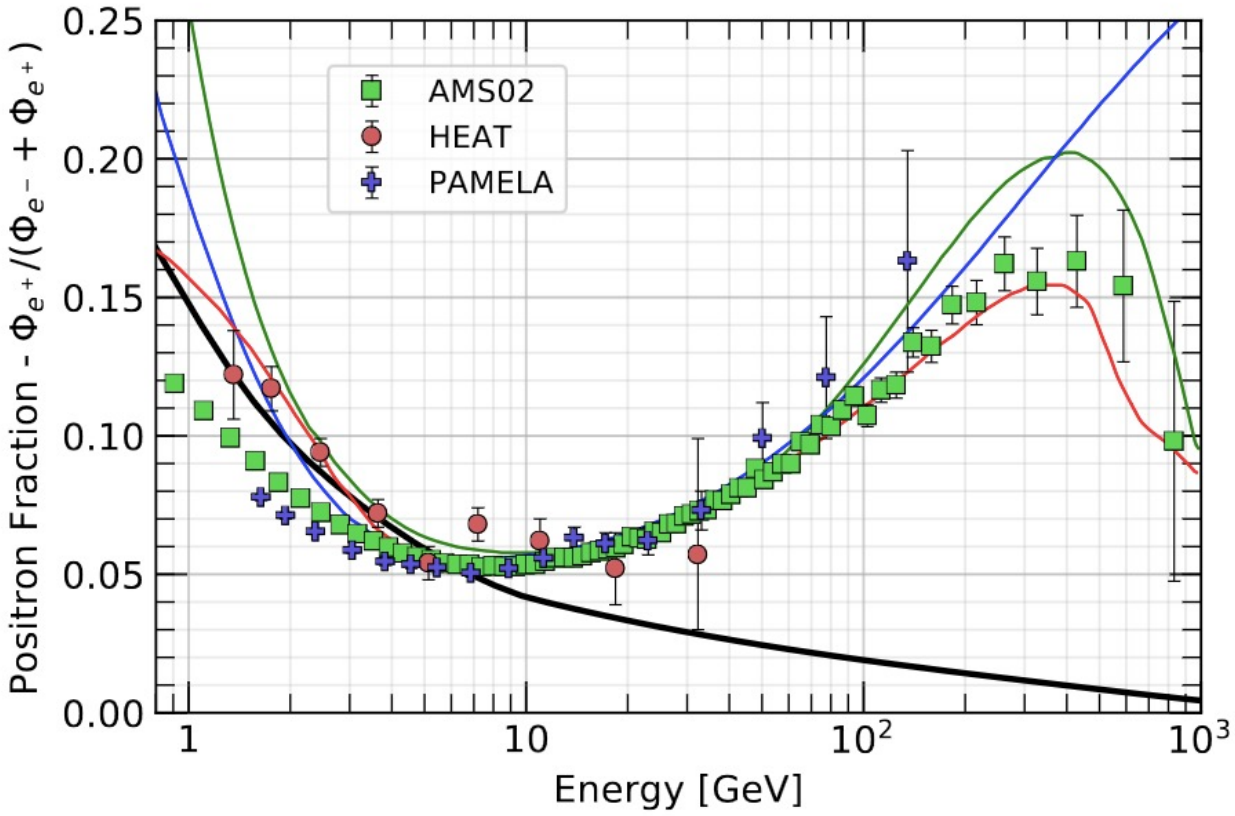

Positron fraction
R. L. Workman et al., 2022

Main mechanisms of production of gamma radiation

All celestial bodies are sources of gamma rays due to the interactions of CRs impinging on their surfaces

Interactions with matter

- Hadronic interactions: inelastic collisions of high-energy protons and nuclei with matter
  - At high energies, all three types of pions are produced with comparable probabilities
  - The neutral pions immediately decay into two gamma rays with a mean life of 8.4×10^{-17}s
    - They can be directly detected or create an electromagnetic shower
  - The charged pions decay into muons and neutrinos with a mean life of 2.6×10^{-8}s
    - Muons decay into electrons/positrons, which can give rise to more electromagnetic showers
  - For $E < 290\mathrm{MeV}$, no pions produced: processes of spallation (breaking into multiple nuclear fragments)
    - De-excitation of excited states leads to gamma-ray lines or a continuous gamma-ray spectrum in the energy range from several hundreds of keV to several MeV

- Bremsstrahlung: interactions of high-energy positrons or electrons with the Coulomb field of a nucleus
  - The energies of the emitted photons are distributed over a continuous spectrum, with energies of X-rays and gamma rays

- Electron-positron annihilation in matter: it leads to the production of two photons
  - If the velocity of positrons is small, bound states composed of an electron and a positron can form
  - They can decay into three photons: continuous spectrum

Main mechanisms of production of gamma radiation

Interactions with photons or radiation fields

- Inverse Compton scattering: a low-energy photon interacts with a high-energy electron/positron and gains energy at the expense of the electron/positron kinetic energy
  - In the Thomson limit (photon energy in the electron rest frame $\ll m_e c^2$), the scattered photon maximum energy is greater than the initial energy by a factor $4\gamma^2$
  - An electron with $\gamma = 1000$ can turn an optical photon into a gamma ray

- Synchrotron radiation: it is emitted when energetic electrons/positrons are bent in a circular orbit, for example due to the presence of a magnetic field
  - Typical synchrotron frequency: $\nu_s = \gamma^2 \frac{eB}{2\pi m_e c}$

Hadronic cross sections

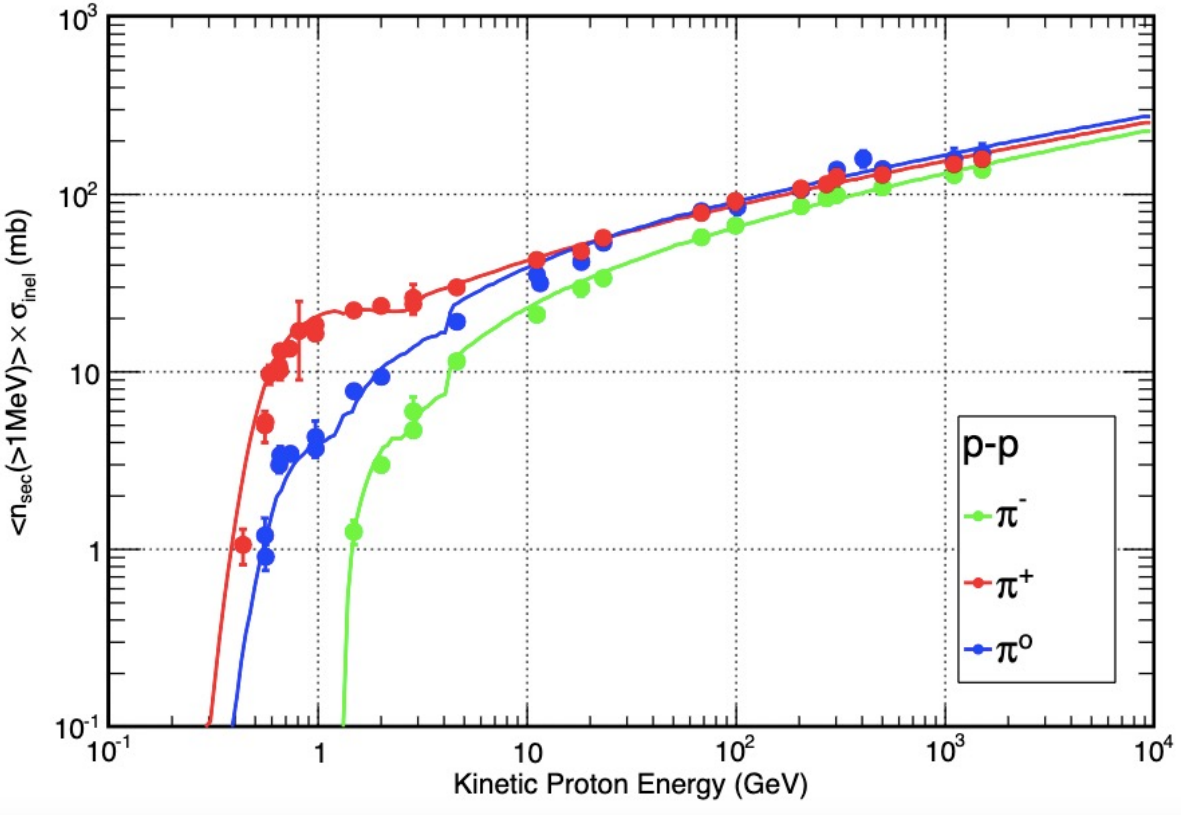

Inclusive cross section for the production of π_0, π_+ and π_-
Lines: FLUKA simulation
Points: data from Dermer, 1986
Figure from Mazziotta et al., 2016

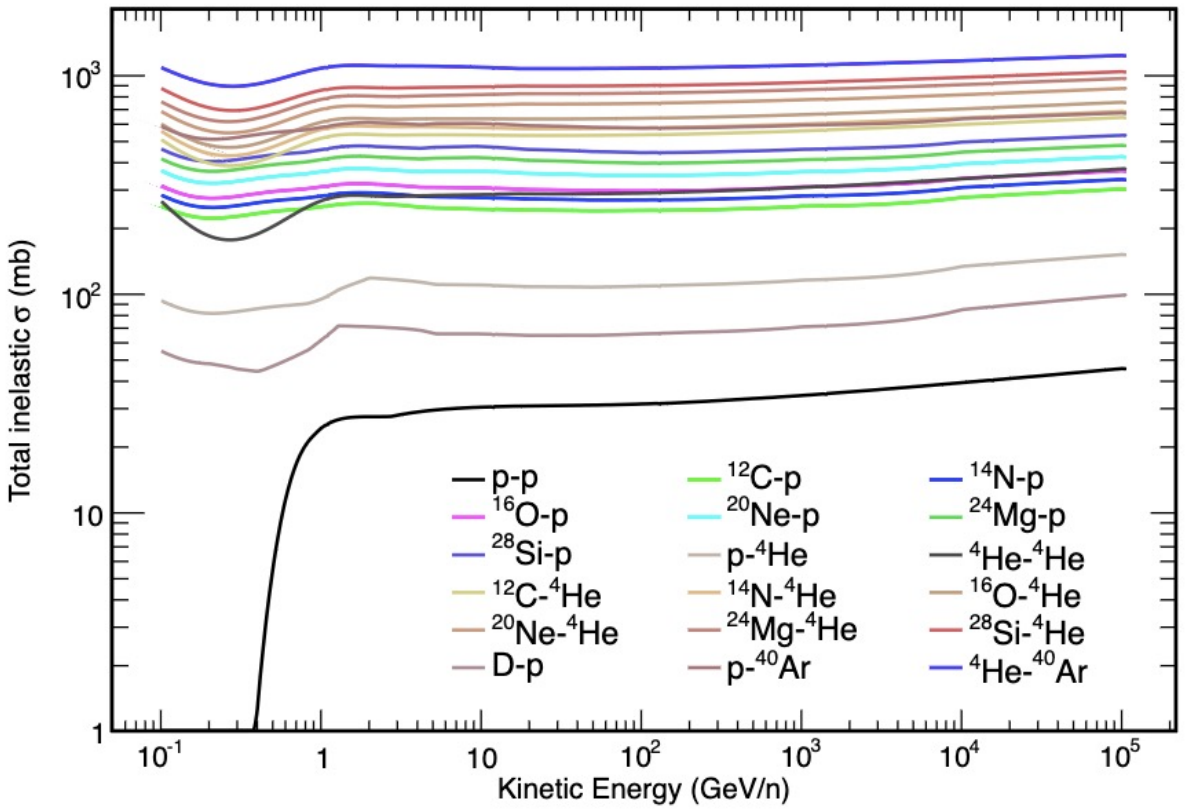

Total inelastic cross sections as a function of the energy per nucleon of the incoming projectile. The plot shows the cross sections for all the projectile-target pairs studied in Mazziotta et al., 2016

Bremsstrahlung and electron-positron annihilation

Bremsstrahlung cross section

$$\frac{d\sigma}{dk} = \frac{4\alpha r_e^2}{k}\left\{\left(\frac{4}{3} - \frac{4}{3}y + y^2\right)\left[Z^2(L_{rad} - f(Z)) + ZL'_{rad}\right] + \right.$$
$$\left. + \frac{1}{9}(1-y)(Z^2+Z)\right\}$$

$$\alpha = \frac{1}{137} \qquad r_e = \frac{e^2}{4\pi\epsilon_0 m_e c^2}$$

$$f(Z) = a^2\left[(1+a^2)^{-1} + 0.20206 - 0.0369a^2 + 0.0083a^4 - 0.002a^6\right]$$

for elements up to uranium

$$a = \alpha Z$$

Element	Z	L_{rad}	L'_{rad}
H	1	5.31	6.144
He	2	4.79	5.621
Li	3	4.74	5.805
Be	4	4.71	5.924
Others	> 4	$\ln(184.15\, Z^{-1/3})$	$\ln(1194\, Z^{-2/3})$

Annihilation cross section in the extreme relativistic limit

$$\sigma = \frac{\pi r_e^2}{\gamma}(\ln 2\gamma - 1)$$

γ = Lorentz factor of the positron

Inverse Compton and synchrotron radiation

- Energy loss rate for Inverse Compton scattering in the Thomson limit:

$$\left(\frac{dE}{dt}\right)_{IC} = \frac{4}{3}\sigma_T c u_{rad}\beta^2\gamma^2$$

$\sigma_T = \frac{8}{3}\pi r_e^2$ is the Thomson cross section, u_{rad} the energy density of the incoming radiation

- Synchrotron radiation: energy loss rate in the ultra-relativistic limit:

$$\frac{dE}{dt} = 2\sigma_T c U_{mag}\gamma^2 \sin^2\alpha$$

$\alpha =$ pitch angle of the high-energy electron/positron in the magnetic field

$U_{mag} = B^2/2\mu_0 =$ magnetic field energy density

Inverse Compton Klein-Nishina cross-section

$$\sigma_{IC}(x) = \sigma_T \frac{3}{4x}\left[\left(1 - \frac{4}{x} - \frac{8}{x^2}\right)\ln(1+x) + \frac{1}{2} + \frac{8}{x} - \frac{1}{2(1+x)^2}\right]$$

$$x = \frac{2E_e\epsilon(1-\beta\cos\theta)}{m_e^2}$$

The FLUKA code

- FLUKA is a general purpose Monte Carlo code for the simulation of hadronic and electromagnetic interactions

- It can simulate with high accuracy the interactions and propagation in matter of about 60 different species of particles, including photons and electrons from 1 keV to thousands of TeV, neutrinos, muons of any energy, hadrons and the corresponding antiparticles of energies up to 20 TeV or up to 10 PeV when it is interfaced with the DPMJET code, neutrons down to thermal energies and heavy ions

- Hadronic interactions in FLUKA below a few GeV are based on resonance production and decay of particles, while for higher energies the Dual Parton Model is used, implying a treatment in terms of quark chain formation and hadronization

- The interactions are simulated in the framework of the PreEquilibrium Approach to NUclear Thermalization model (PEANUT), including the Gribov-Glauber multi-collision mechanism followed by the pre-equilibrium stage and eventually equilibrium processes (evaporation, fission, Fermi break-up and gamma de-excitation)

Abundances in C-type and S-type asteroids

Element	Abundance in C-type asteroids (%)	Abundance in S-type asteroids (%)
H	2.02	-
C	3.45	-
O	46.4	35.70
Mg	9.70	14.1
Al	0.865	1.06
Si	10.64	17.1
S	5.41	2.0
Ca	0.926	1.22
Fe	18.2	27.2
Ni	1.10	1.71

Compositions from K. Lodders and B. Fegley, 1998

FLUKA simulation

- $Y_i(E_\gamma|E_k, r)$: yield (in units of GeV^{-1}) of gamma rays produced by the interaction of the *i*-th CR species with energy E_k with the body surface of radius r
- The primary kinetic energy values are taken on a grid of 81 equally spaced values in a logarithmic scale, from 100 MeV/n up to 10 TeV/n

$$Y_i(E_\gamma|\ E_k, r) = \frac{N_i(E_\gamma|\ E_k, r)}{N_i(E_k)\Delta E_\gamma}$$

- $N_i(E_k)$ = n. of primaries of the *i*-th species with energy E_k
- $N_i(E_\gamma|E_k, r)$ = n. of photons with energy between E_γ and $E_\gamma + \Delta E_\gamma$ produced by the primaries of the type *i* with kinetic energy E_k impinging on the asteroid of radius r, escaping from the asteroid

- The gamma-ray energy values go from 0.1 MeV up to 100 MeV with a spacing of 32 bins per decade and from 100 MeV up to 10 TeV with a spacing of 8 bins per decade

FLUKA simulation

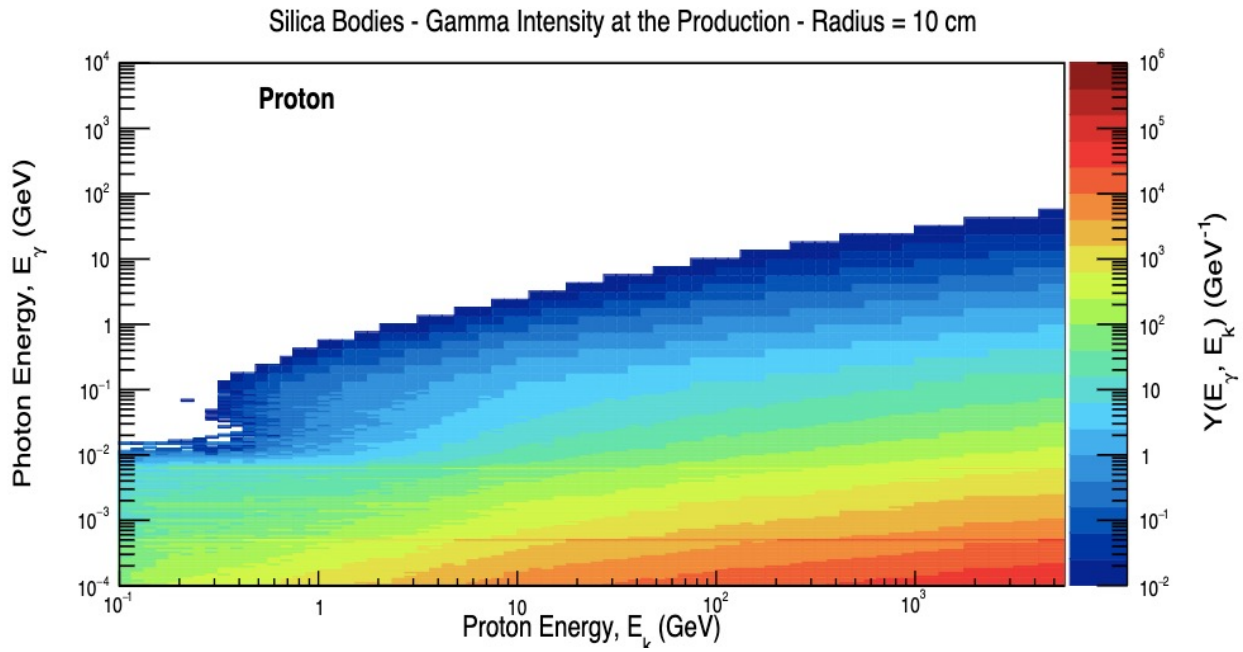

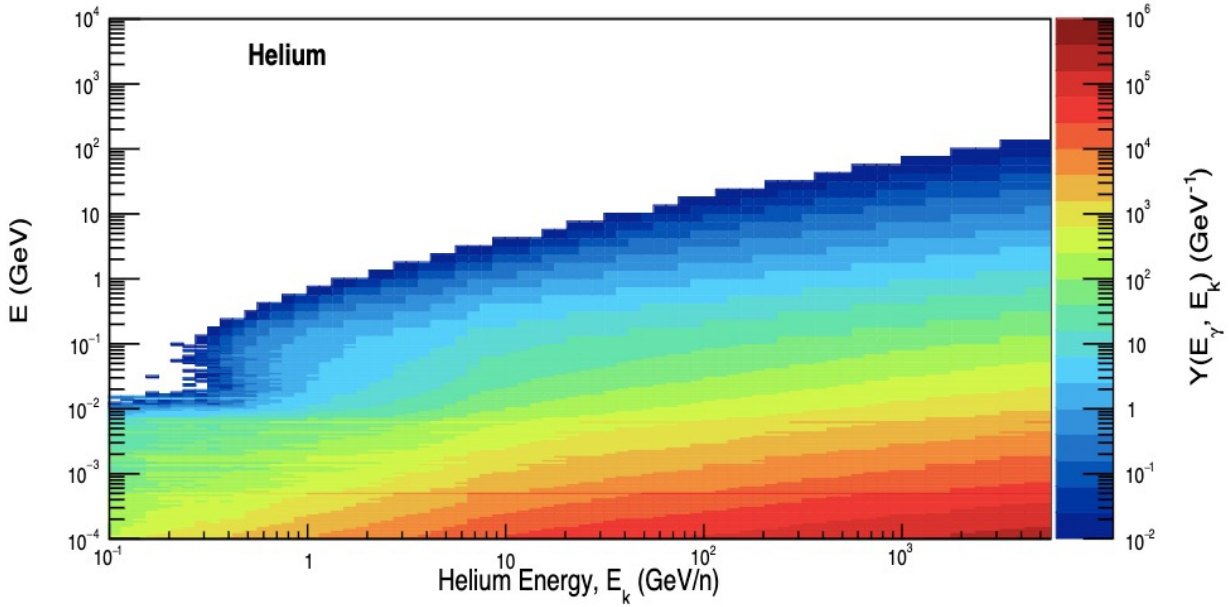

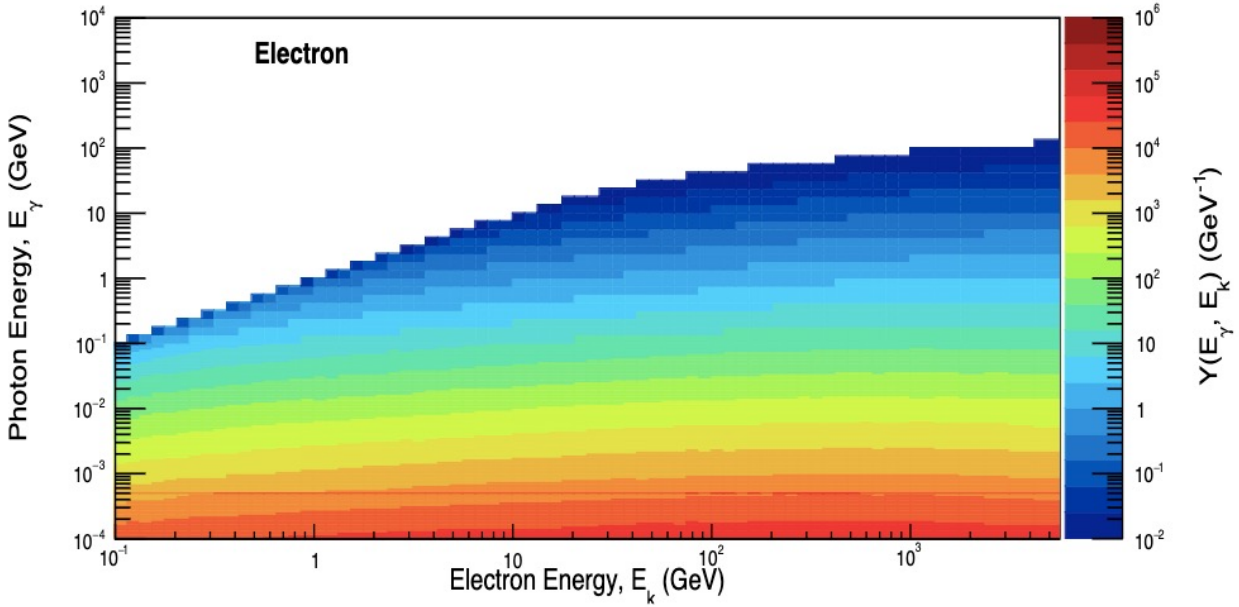

FLUKA simulation

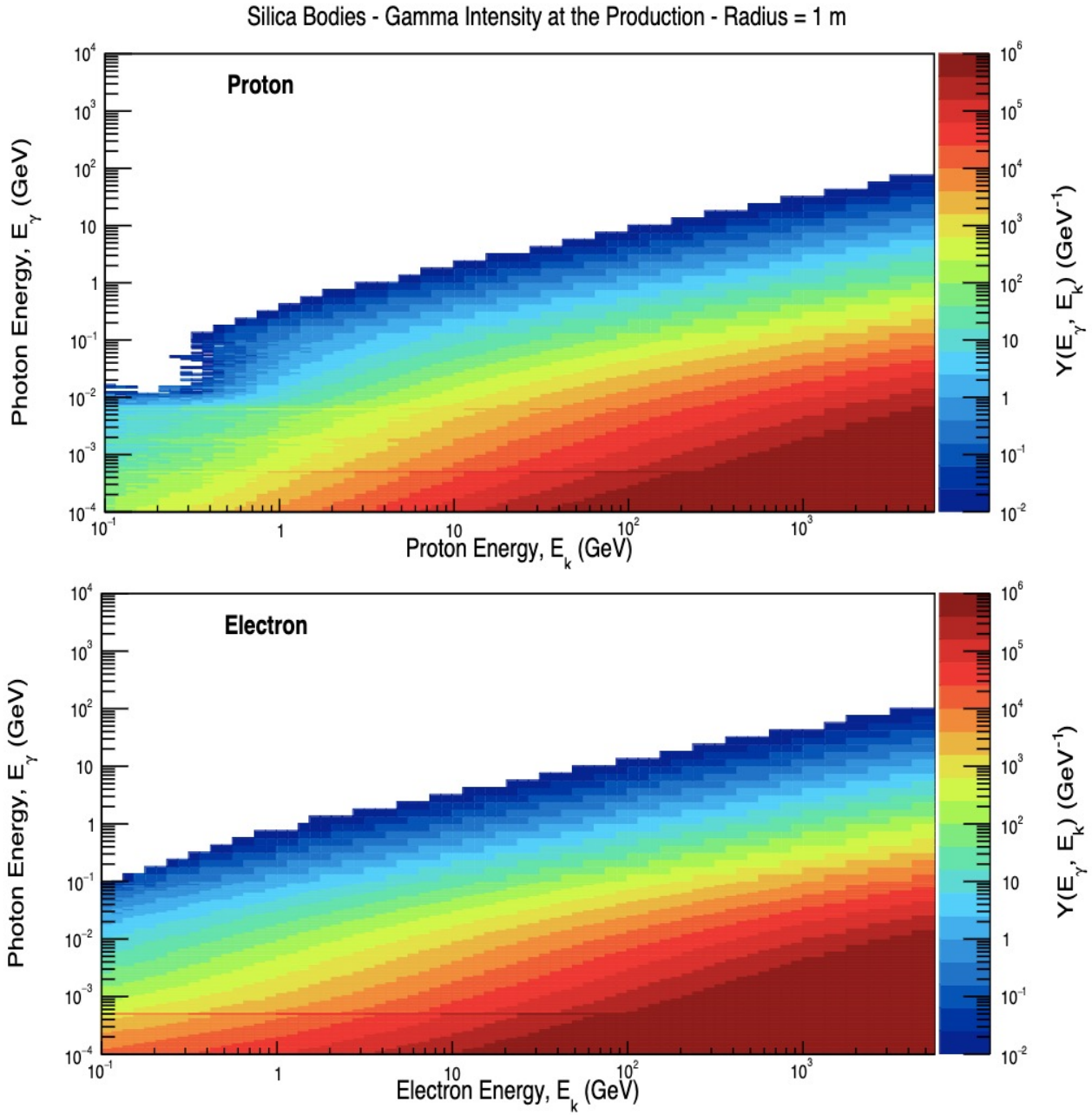

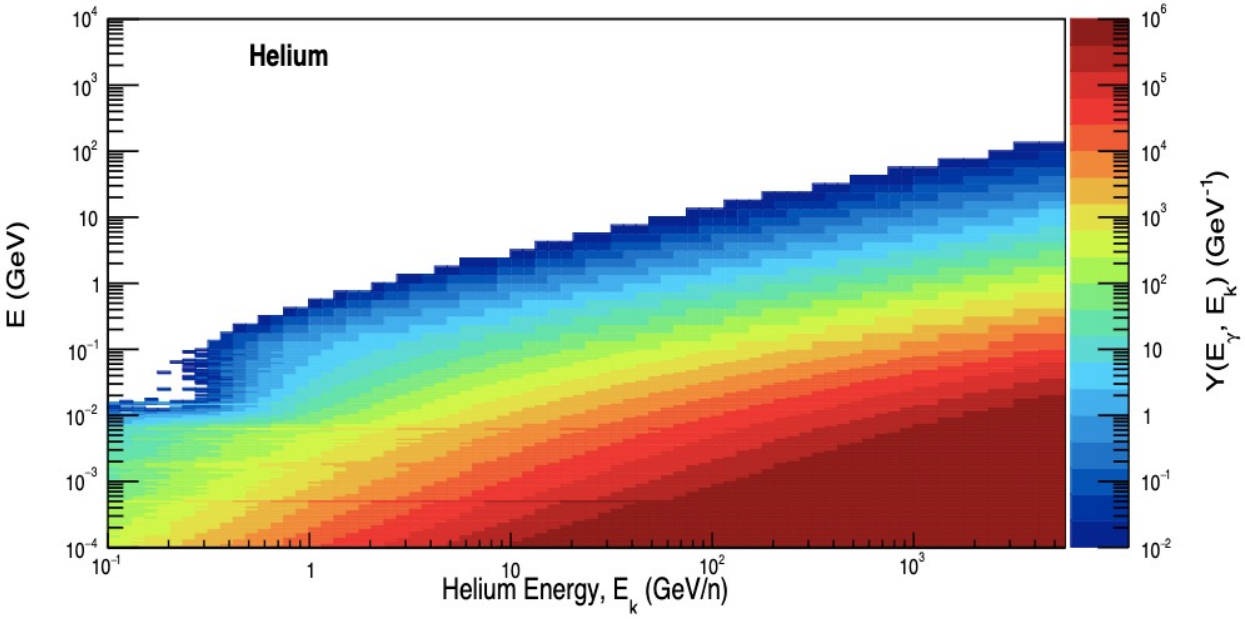

FLUKA simulation

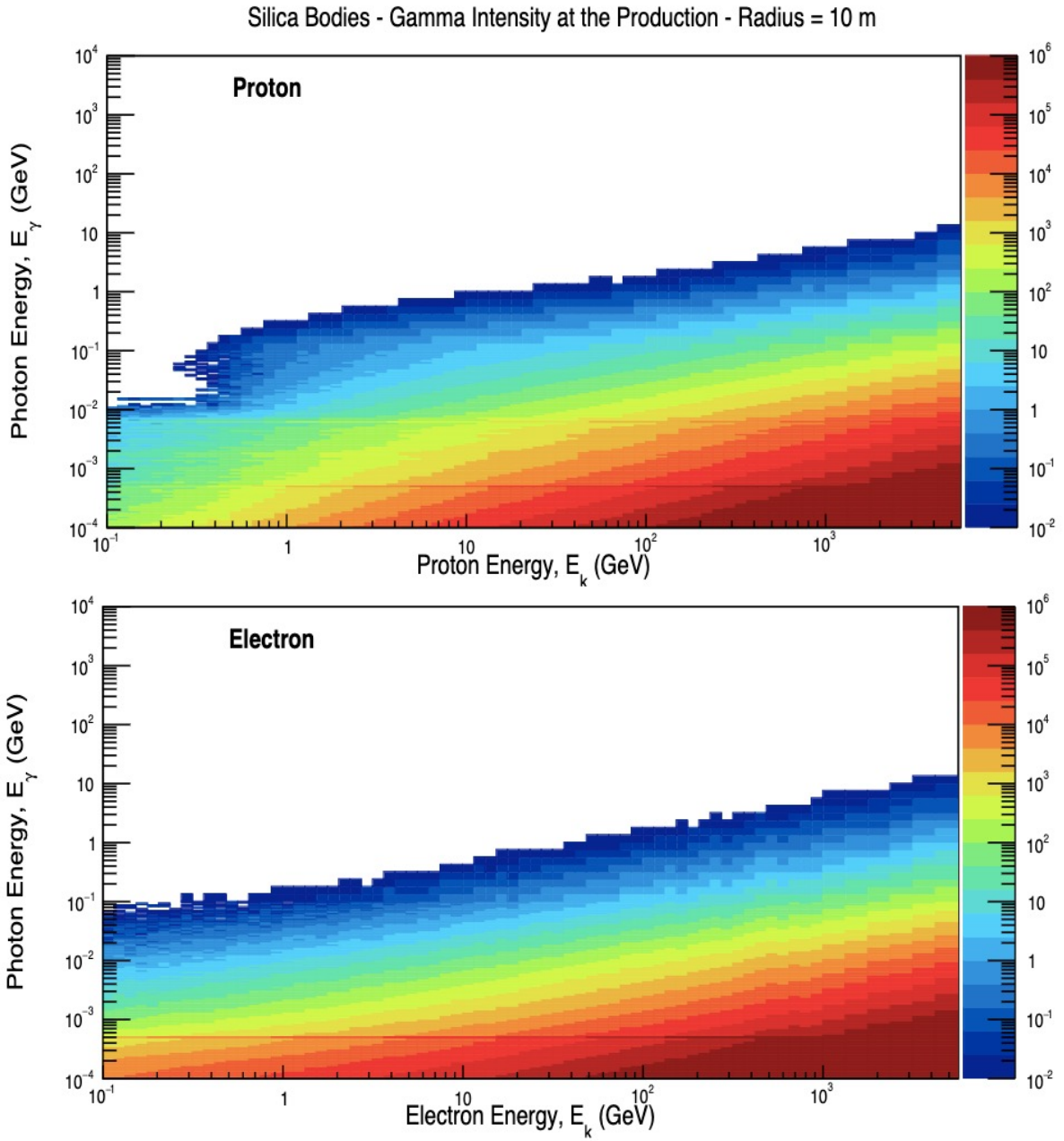

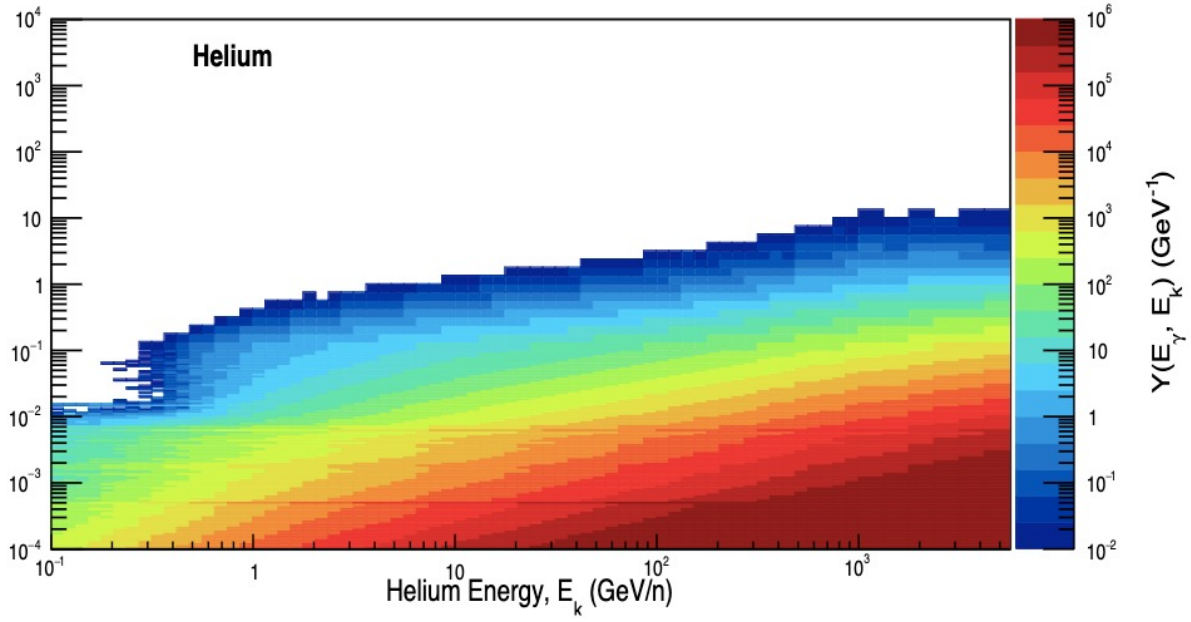

FLUKA simulation

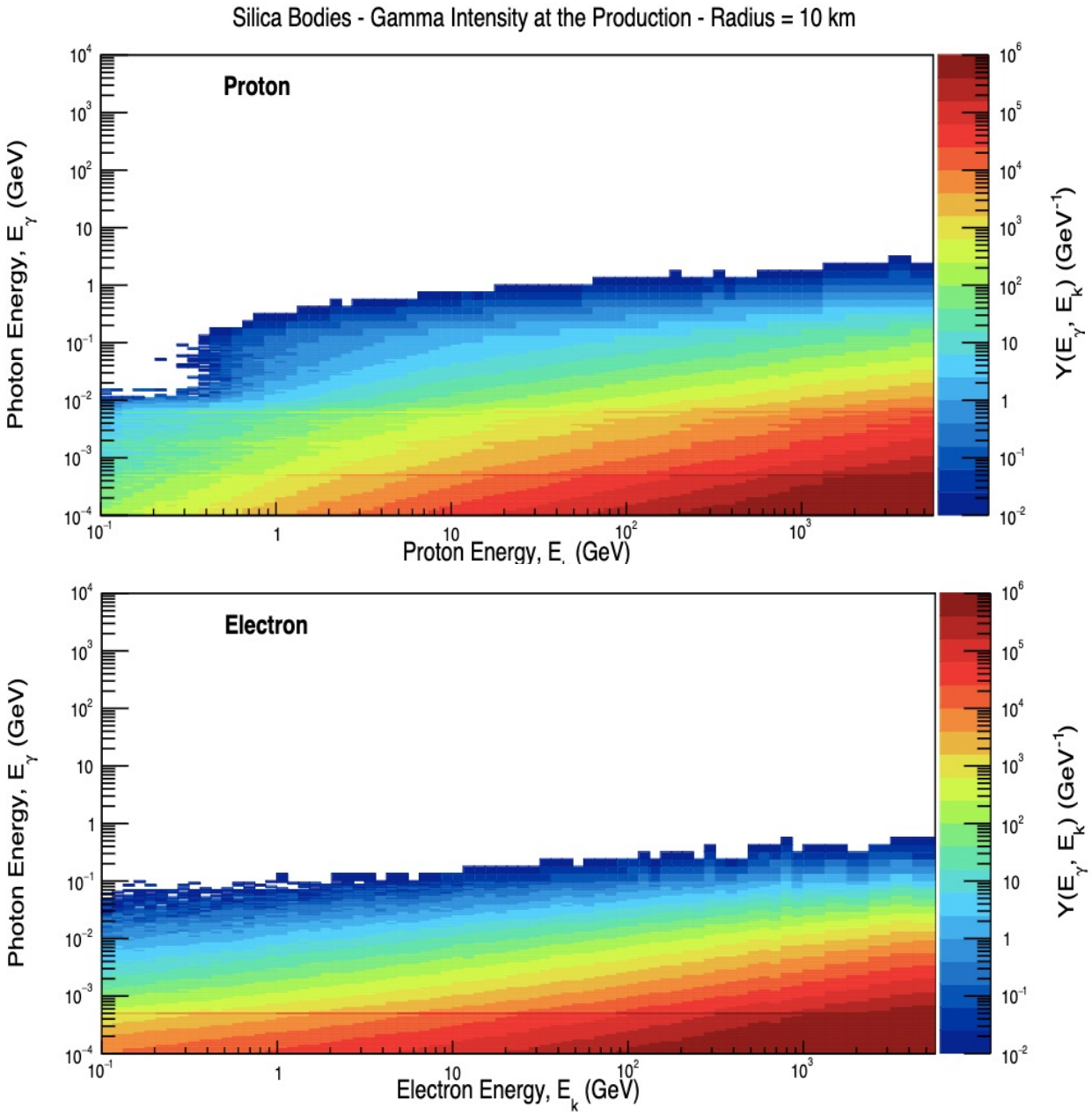

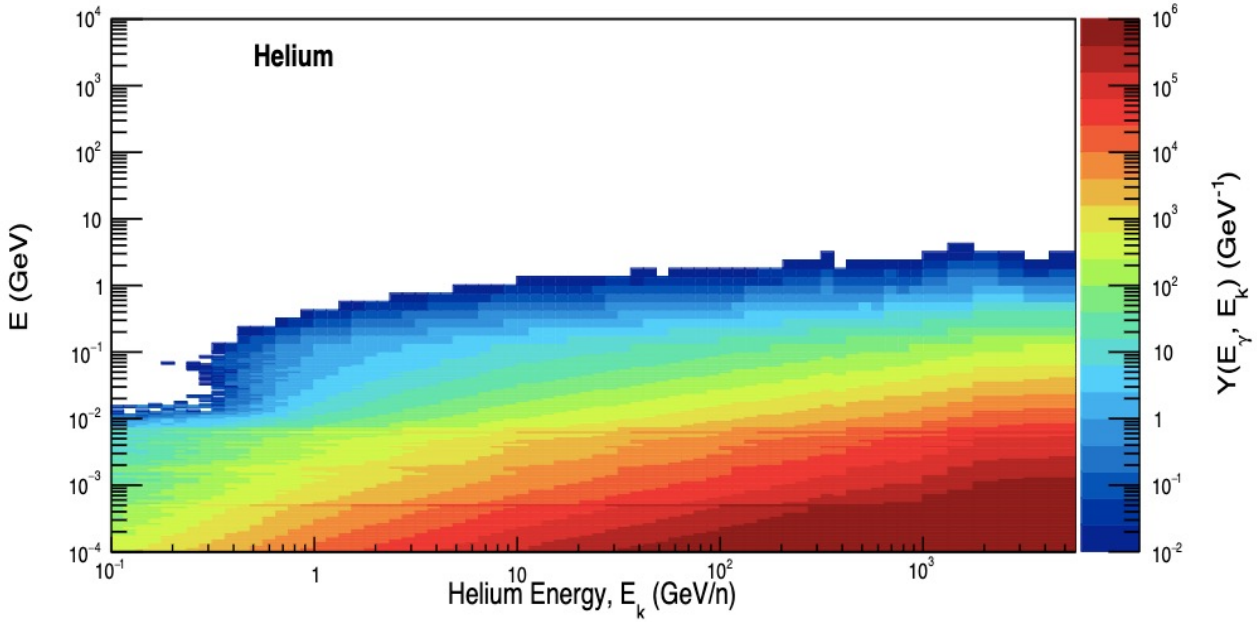

- Regions of high photon energies tend to be less populated as the asteroid size increases: CR nuclei can penetrate down to depths of a few tens of g/cm^2 while the radiation length is shorter: when the asteroid size is larger than both these characteristic lengths, the gamma-ray production becomes independent of the size and many gamma rays produced inside the body are not able to escape from the asteroid, so that the yield decreases
- For energies less than ~ 300 MeV, the gamma-ray yield produced in the interactions of protons and He nuclei with the asteroid tends to vanish for photon energies above 10 MeV: this is below the threshold for activating the π^0 production
- For photon energies less than 10 MeV, the yield comes from de-excitation of nuclear fragments in excited energy levels produced in collisions
- In all plots, some horizontal lines are clearly visible, corresponding to characteristic lines related to the asteroid composition (0.511 MeV: e^+-e^- annihilation)

FLUKA simulation

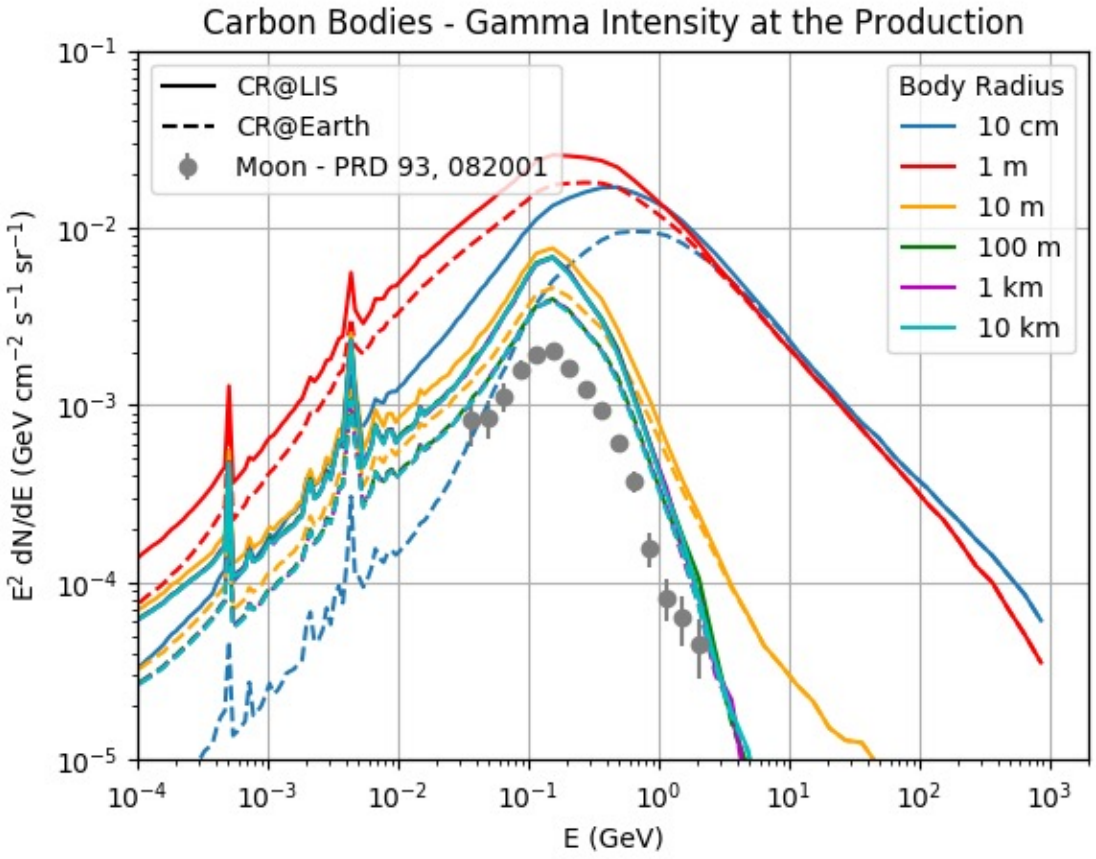

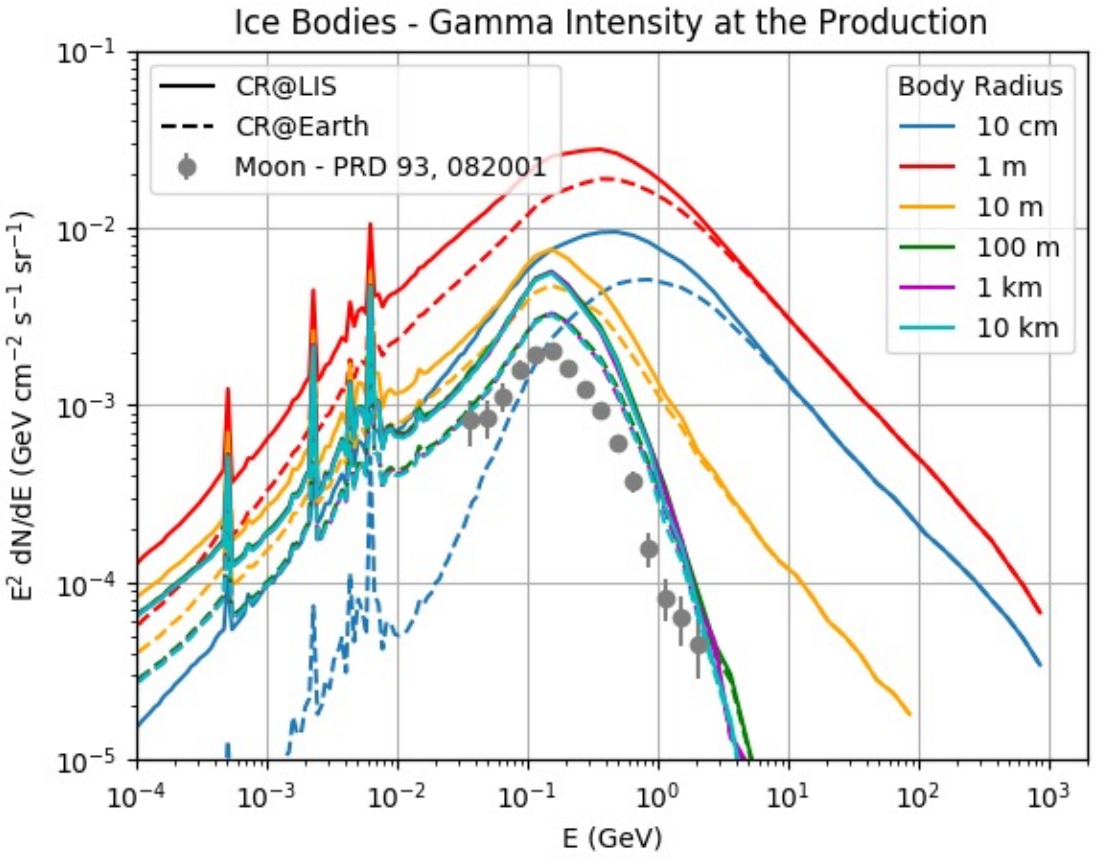

- The line at 2.2 MeV, which is clearly visible in the ice bodies, is due to neutron capture by hydrogen nuclei, with the production of a deuterium nucleus and the emission of a gamma ray

FLUKA simulation

Contributions to the gamma-ray intensities from individual CR species impinging on silica bodies

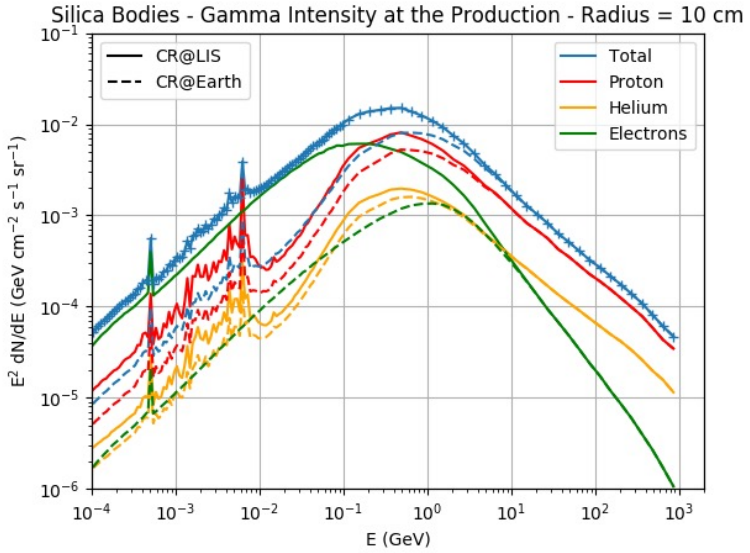

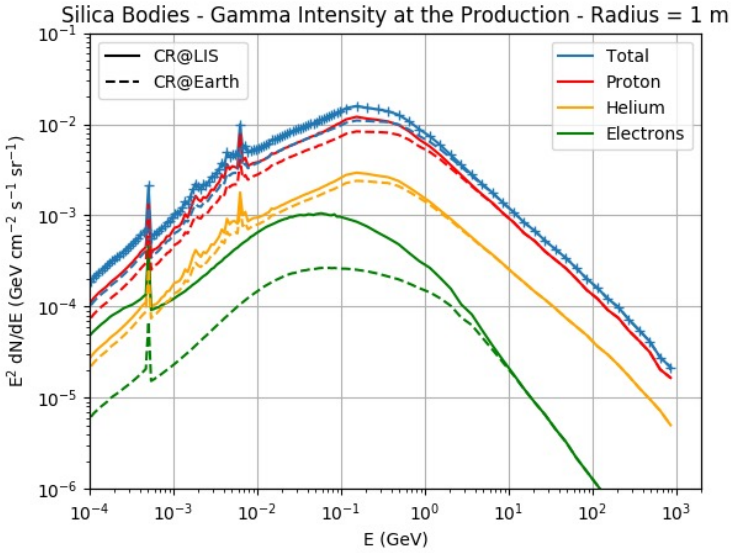

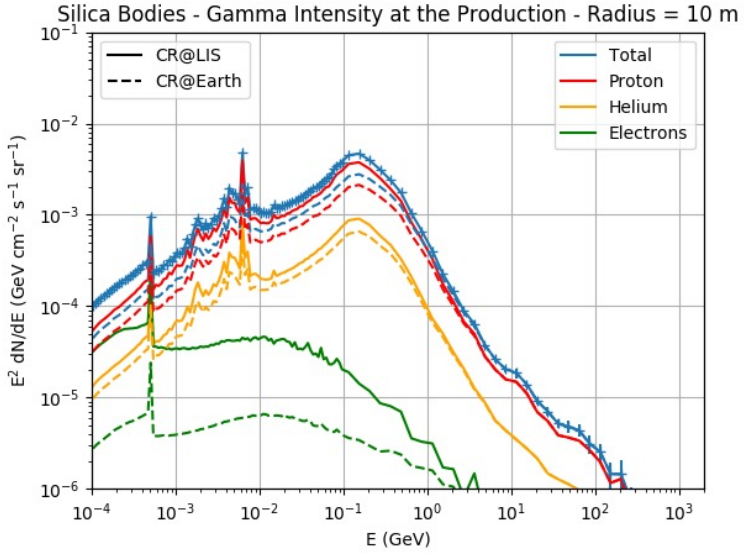

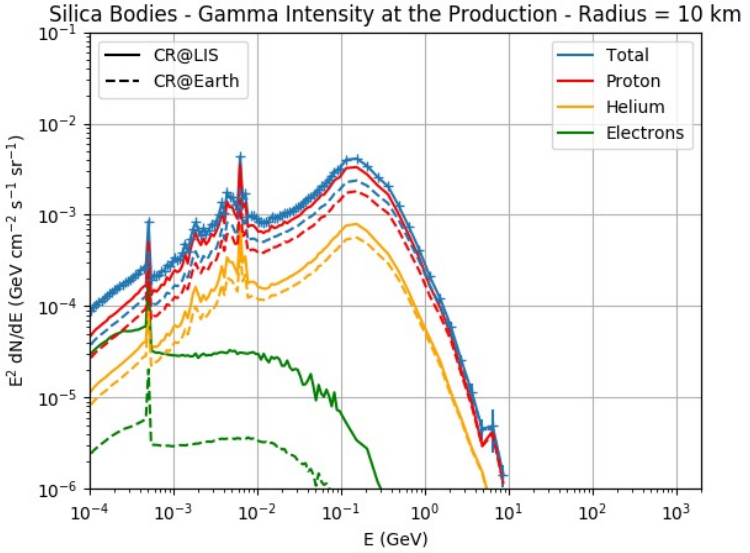

- The average energy of gamma rays produced by each CR species decreases as the asteroid radius increases
- This feature becomes relevant for $r > 1$ m
- Correspondingly, the gamma-ray intensities at production from each species become softer
- The contribution to the gamma-ray intensity given by electrons is characterized by only one line at 0.511 MeV
- The contribution to the gamma-ray intensity given by protons and He nuclei is characterized also by all lines produced in de-excitations of nuclear fragments created in the interactions with the asteroids
- The error bars in the plots represent the statistic uncertainties due to the finite number of CR events used in the simulation to evaluate the yields

FLUKA simulation

Integral of the intensity above 0.1 GeV as a function of the asteroid radius for different classes of asteroids

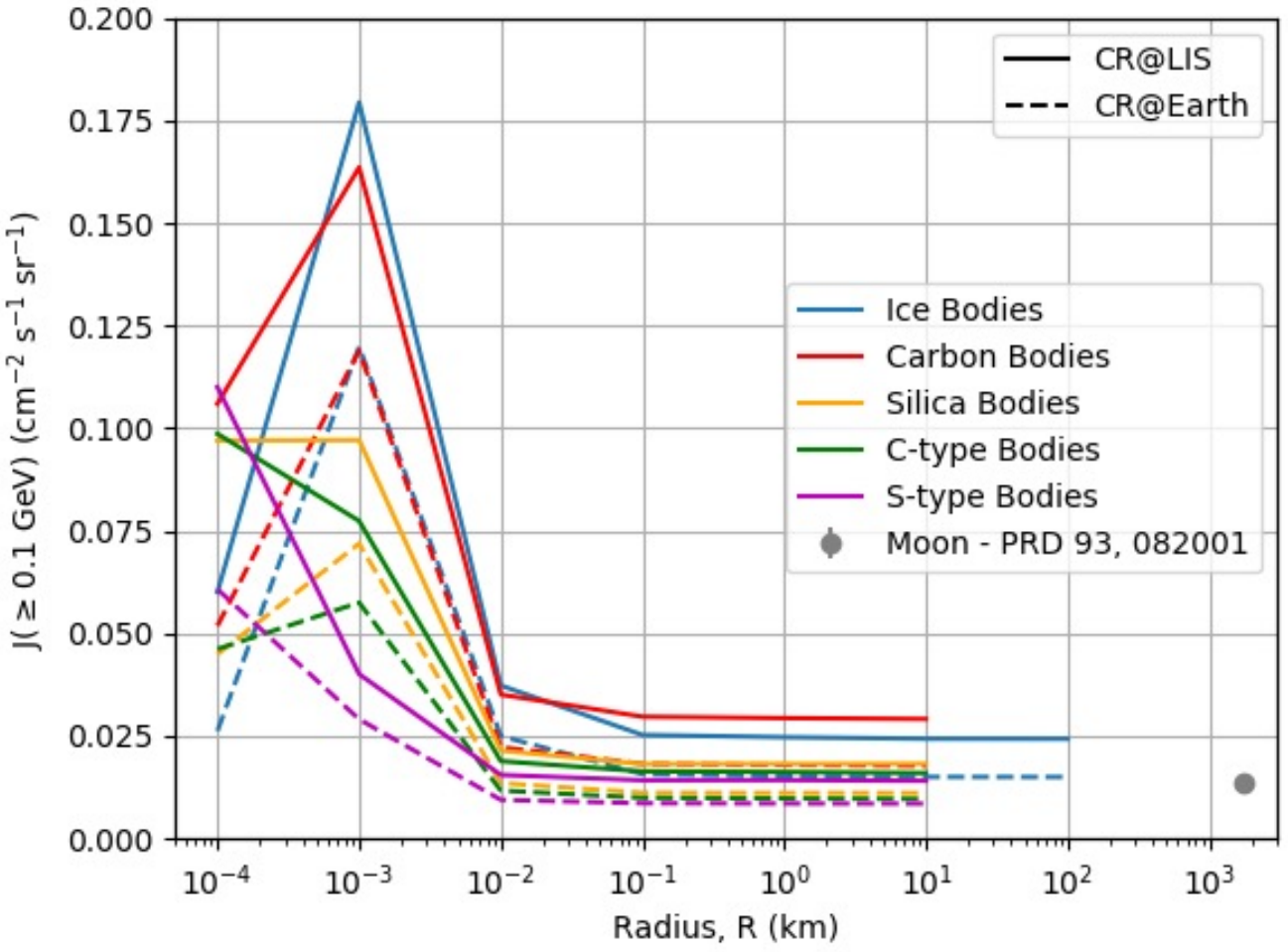

- The intensity at the production site drops for radii smaller than 1 m, since the asteroid size becomes comparable or smaller than the typical interaction length in the simulated materials, which are of the order of tens of cm

- For r > 10 m, the shapes of the spectra (and consequently the integral of the intensity above 0.1 GeV) do not depend on the asteroid radius and are similar to the shape of the gamma-ray intensity from the Moon

Gamma-ray asteroid flux at the Earth

$$\phi_\gamma(E_\gamma, d, r > r_0) = \int_{r_0}^{r_1} \frac{\pi r^2}{d^2} I_\gamma(E_\gamma, r) \frac{dN}{dr} dr$$

- $d = 2.7$ AU, $r_1 \sim 500$ km
- dN/dr given by the model proposed at the beginning of the presentation: JPL catalog for $r > 1.25$ km, extrapolated Durda et al. model for $10\ \text{cm} < r < 1.25$ km

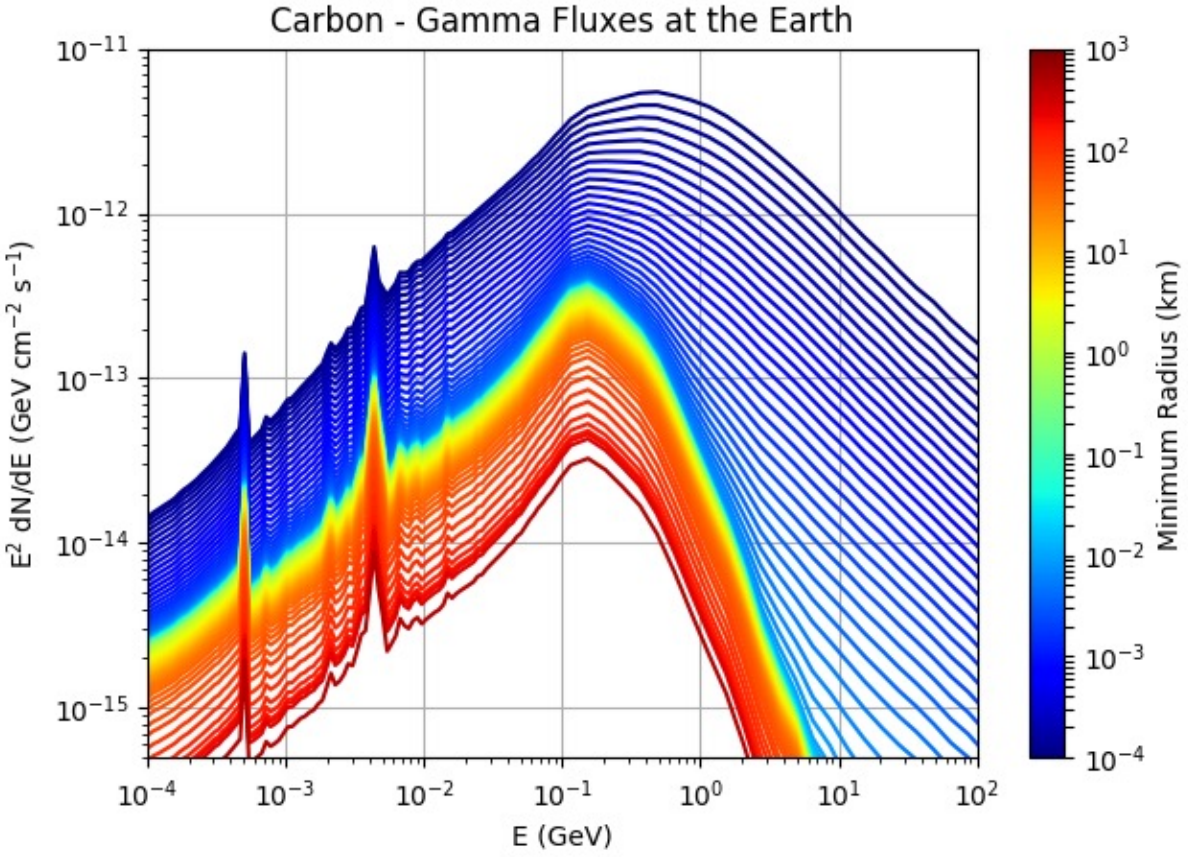

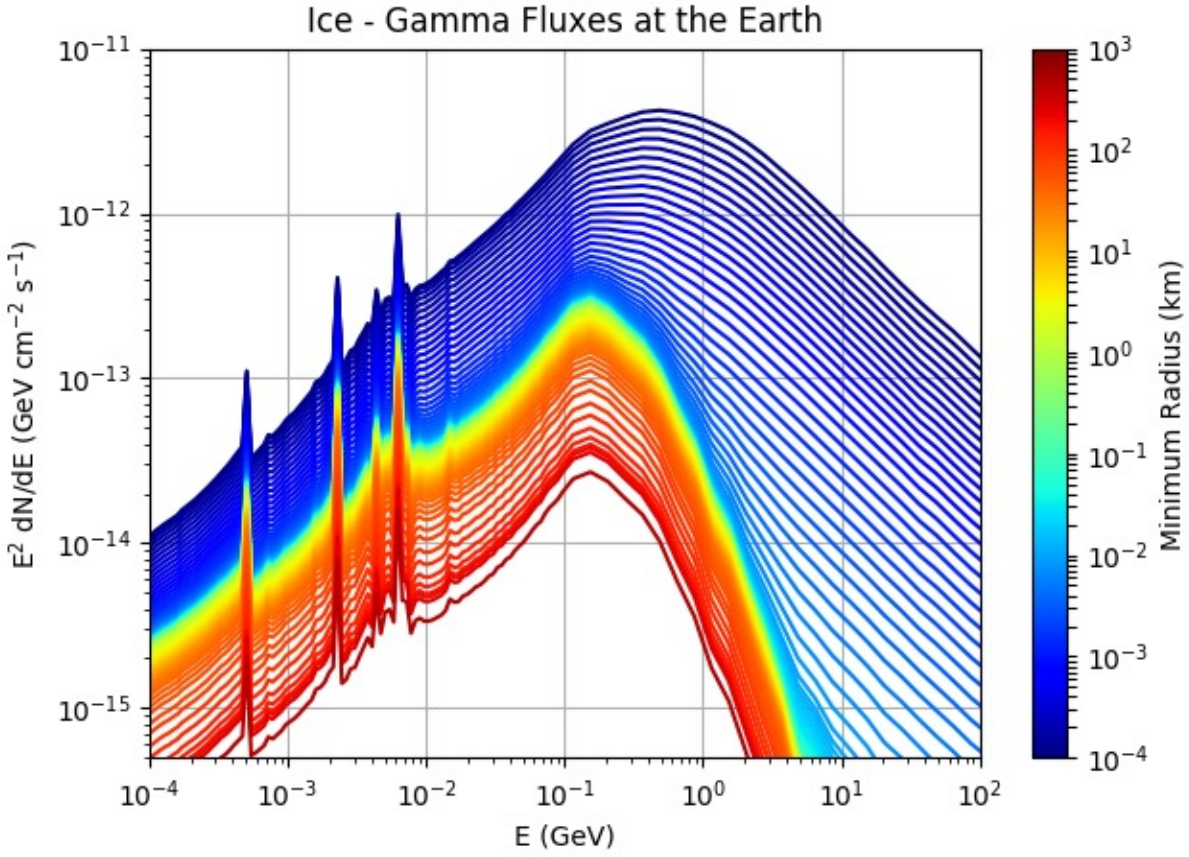

Gamma-ray asteroid flux at the Earth

- Assuming that the gamma-ray intensity does not depend on the asteroid radius, that it is the same as from the Moon and that asteroid size distribution follows a power-law with index α, the ratio between asteroid total flux and Moon flux is equal to

$$\frac{\phi}{\phi_{\leftmoon}} = \begin{cases} a \dfrac{1}{R_{\leftmoon}^2} \dfrac{D_{\leftmoon}^2}{d^2} \times \dfrac{r_1^{3-\alpha} - r_0^{3-\alpha}}{3-\alpha} & \text{for } \alpha \neq 3 \\ a \dfrac{1}{R_{\leftmoon}^2} \dfrac{D_{\leftmoon}^2}{d^2} \times \log \dfrac{r_1}{r_0} & \text{for } \alpha = 3 \end{cases}$$

This work

$$\frac{\phi}{\phi_{\leftmoon}} = \begin{cases} a \dfrac{1}{R_{\leftmoon}} \dfrac{D_{\leftmoon}^2}{d^2} \times \dfrac{r_1^{2-\alpha} - r_0^{2-\alpha}}{2-\alpha} & \text{for } \alpha \neq 2 \\ a \dfrac{1}{R_{\leftmoon}} \dfrac{D_{\leftmoon}^2}{d^2} \times \log \dfrac{r_1}{r_0} & \text{for } \alpha = 2 \end{cases}$$

Moskalenko et al., 2008

- Assuming a population of asteroids with radii between r_0 = 10 cm and r_1 = 470 km, the model in this work predicts an asteroid flux from two to six orders of magnitudes lower than the flux calculated in Moskalenko et al., 2008, depending on the index α of the power-law describing the asteroid size distribution

Details on the LAT

Tracker

The thickness of the tungsten layers was optimized to minimize bremsstrahlung energy losses and multiple scattering of positrons and electrons at low energies, and to maximize the conversion probability at high energies, where the photon flux has a lower rate. For this reason, the TKR was segmented into a *front* section and a *back* section. The front section consists of the top 12 planes, made of thin tungsten foil converters (0.03 radiation length), while the back section consists of the left 4 planes, equipped with thicker tungsten converters (0.18 radiation length)

Calorimeter

Each crystal is read out by two photodiodes, one at each side, which provide three spatial coordinates: the first two are given by the geometrical location of the crystal in the array, while the third is given by measuring the light yield asymmetry at the ends of the crystal along its longitudinal dimension. The level of segmentation described above enables energy measurements up to a TeV. In addition, it allows spatial imaging of the shower and accurate reconstruction of its direction

Anticoincidence detector

It is made of plastic scintillators hermetically enclosing the calorimeter and the tracker. The ACD must avoid "self-vetoes" caused by the *backsplash* on the ACD itself of secondary particles produced in the calorimeter, which becomes important for energies above ~ 10 GeV. To meet this requirement, the ACD is segmented into 89 tiles of scintillators: an array of 5 × 5 scintillators is located on the top, while each of the four sides are equipped with 16 tiles. The segmentation provides spatial information which can be correlated with the signal from the calorimeter and tracker modules

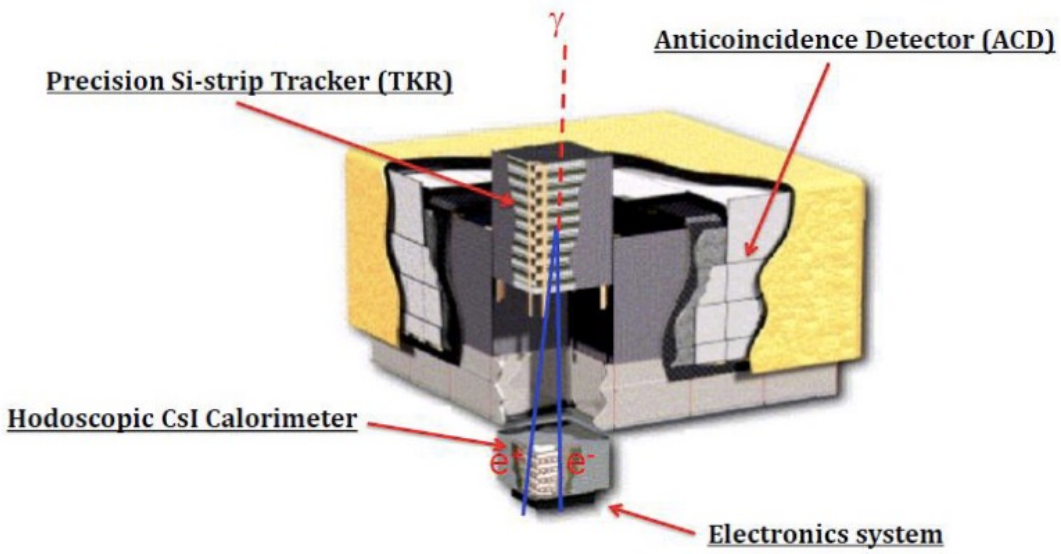

Details on the LAT

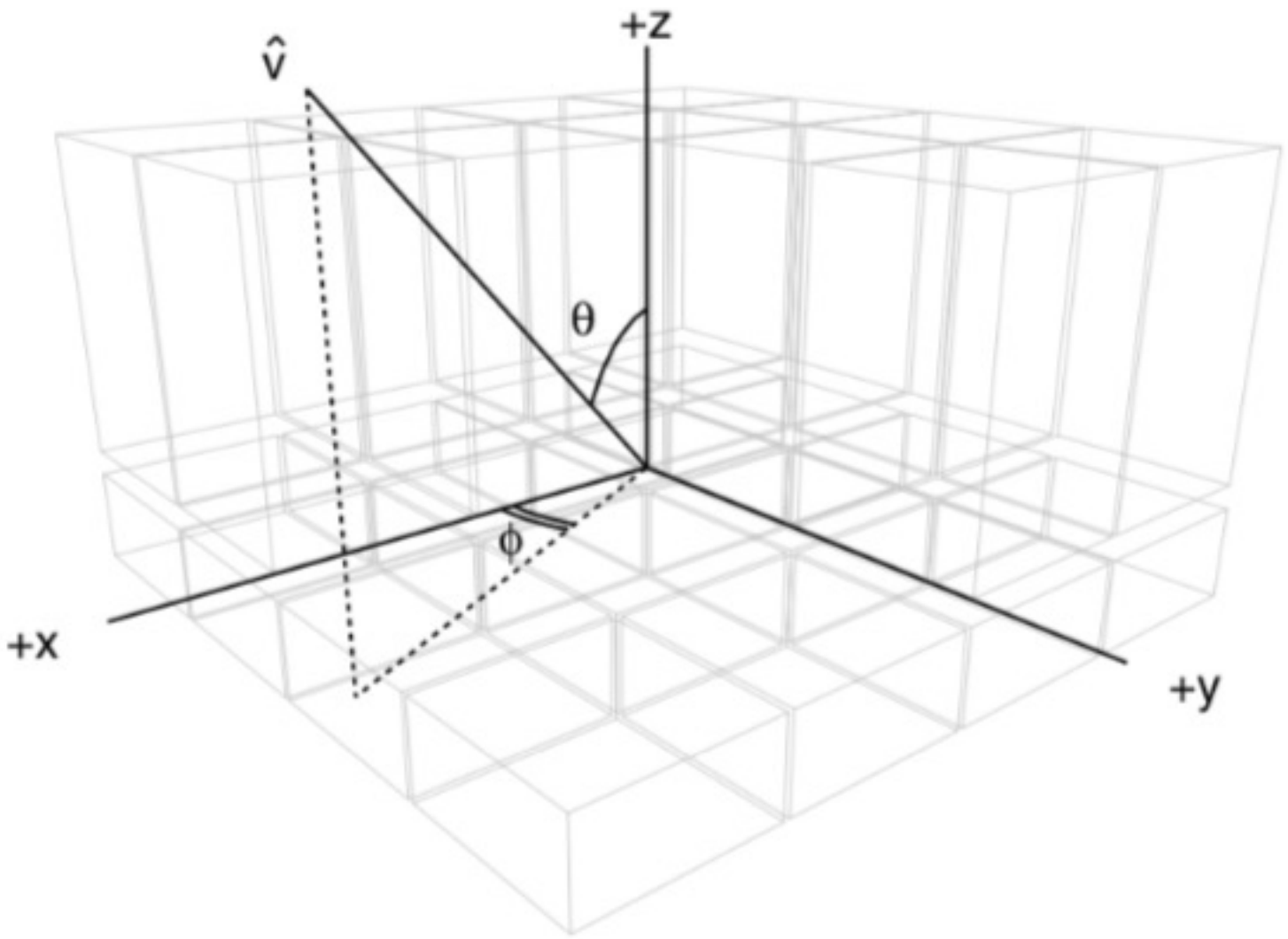

LAT reference frame (M. Ackermann et al., 2012)

Instrument Response Functions (IRFs)

The data analysis cannot be performed without a detailed knowledge of the instrument performances. Such performances are described by the so-called "Instrument Response Functions" (IRFs) and are determined by three main factors: the event reconstruction algorithms, the hardware design and the event quality selection together with the background rejection. The detected photons are sorted into several classes, each of which is suitable for a different kind of analysis and is characterized by its own set of IRFs.

The IRFs describe the performances of the instrument in terms of photon incidence angle, energy, conversion point within the instrument and other parameters. The differential count rate measured by the instrument per unit energy and solid angle can be written as the convolution of the "true" differential flux per unit area of photons entering in the instrument with the IRFs, as in the following:

$$\frac{dN}{dtdEd\hat{u}}(E,\hat{u},t) = \int dE'd\hat{u}'\mathcal{R}(E,\hat{u}|E',\hat{u}',t)\frac{dN}{dtdE'd\hat{u}'dS}(E',\hat{u}',t)$$

where the quantities E' and $\hat{u}'$ represent the true photon energy and direction, while E and $\hat{u}$ represent the same quantities reconstructed. $\mathcal{R}$ represents the IRFs, which are the mapping between the incoming photon flux and the detected events. The IRFs can be factorized into three terms:

- Effective Area $\mathcal{A}(E',\hat{u}')$: it represents the detection efficiency (expressed as an area) for photons of true energy E' and arrival direction $\hat{u}'$
- Point Spread Function (PSF) $\mathcal{P}(\hat{u}|E',\hat{u}')$: it represents the probability for a photon of true energy E' and arrival direction $\hat{u}'$ to be reconstructed with direction $\hat{u}$
- Energy dispersion $\mathcal{D}(E|E',\hat{u}')$: it represents the probability that a photon with true energy E' and arrival direction $\hat{u}'$ is reconstructed with energy E

The IRFs are generated from a full Monte Carlo simulation of the instrument, using the software Geant4. In the simulation, the detector is immersed inside an isotropic, uniform flux of particles. A large number of photons and background particles with all possible energies and inclination angles are simulated, and the reconstruction algorithms are applied to the simulated data set to quantify the accuracy in the reconstruction of gamma-ray energies and directions, the gamma-ray detection efficiency and the CR contamination.

Effective area

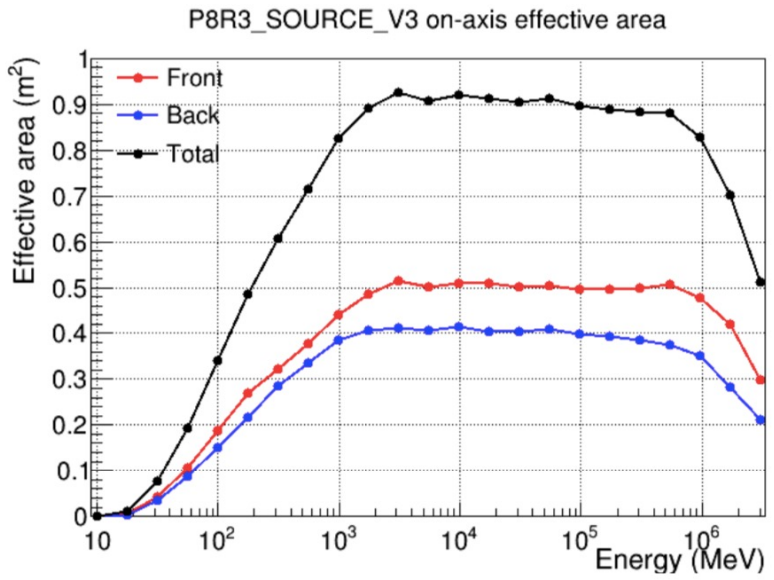

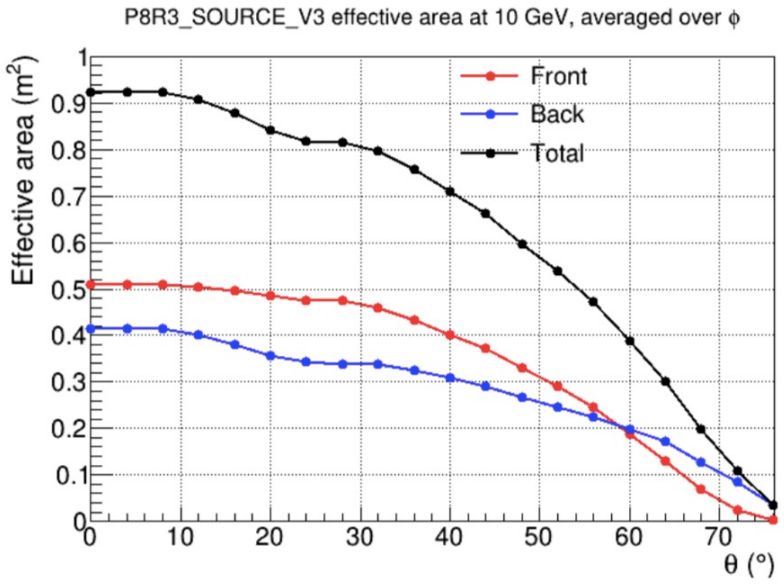

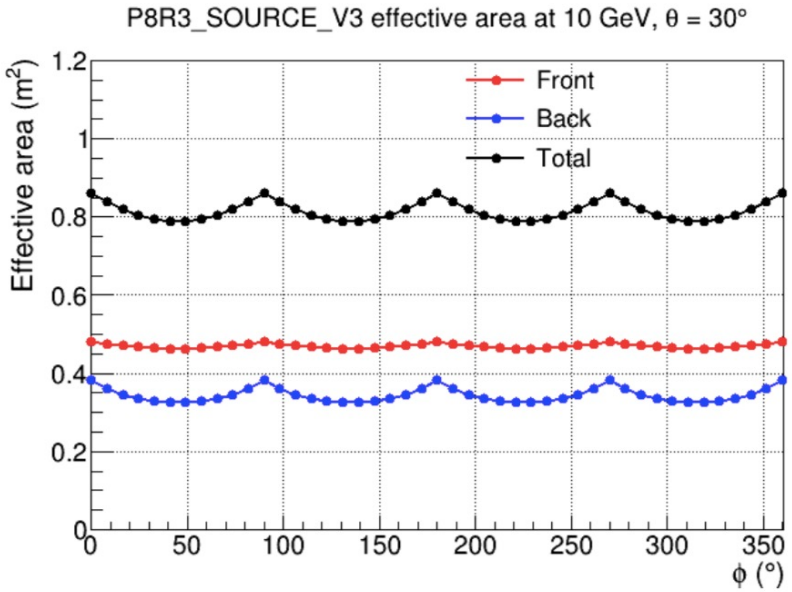

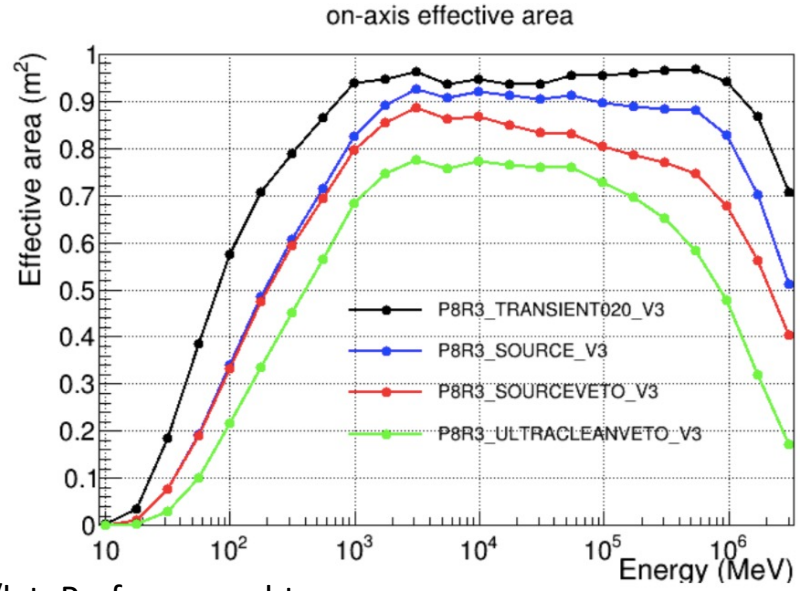

https://www.slac.stanford.edu/exp/glast/groups/canda/lat_Performance.htm

At low energies, the effective area increases with energy, following the behavior of the pair production cross section. For photon energies between a few GeV and a few hundeds GeV the effective area is roughly constant, as the cross section. Then, in the TeV region, the effective area decreases as the *backsplash* effect reduces the detection efficiency.

The effective area is maximum for on-axis incidence and decreases with increasing off-axis angles, since photons crossing the LAT with high on-axis angle have less probability of generating a trigger.

The variations of the effective area with the azimuthal angle are less than 10%, which allows for averaging the effective area over the azimuthal angle.

The increasing quality of reconstructed photons is reached at the expenses of the efficiency, in particular at high energies.

PSF and energy resolution

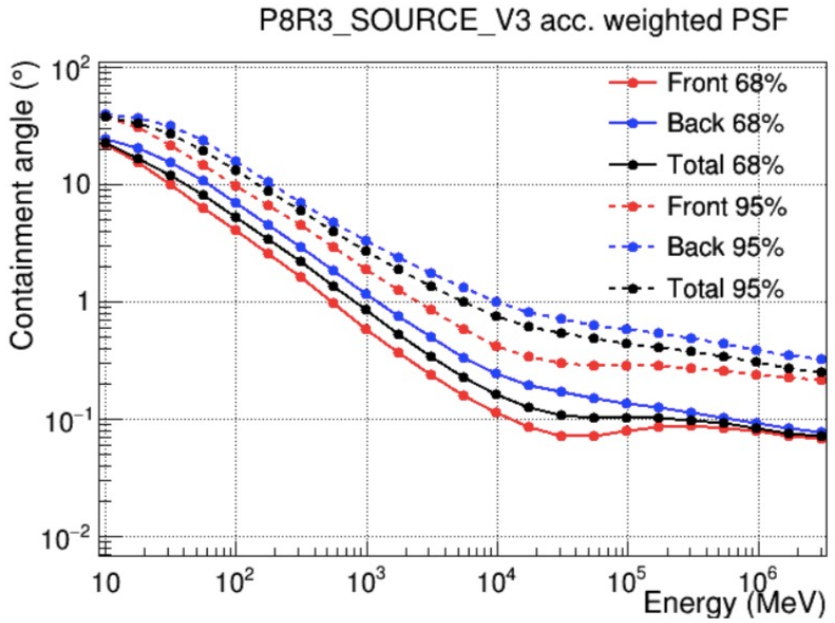

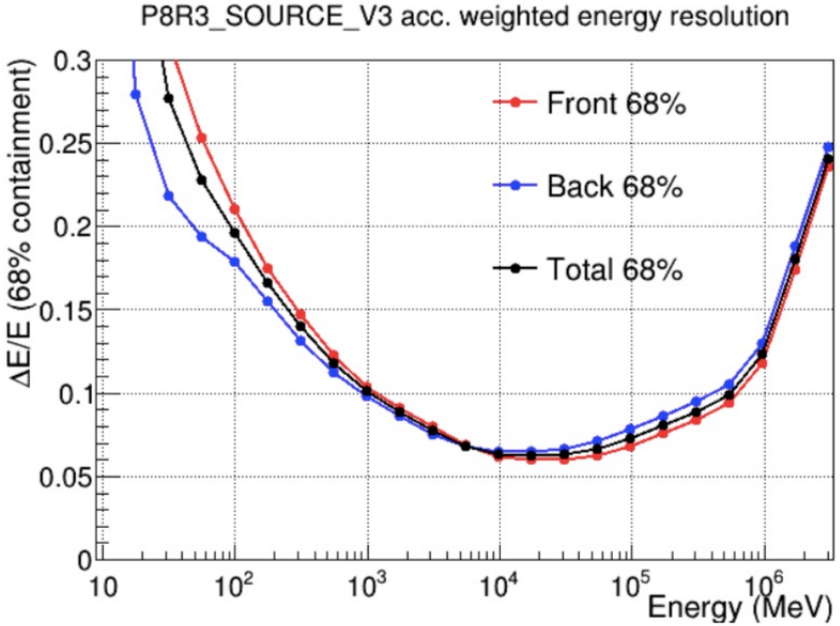

The PSF describes the LAT angular resolution and is derived from Monte Carlo simulations. From the simulated data it is possible to derive the angle θ between the true photon direction $\hat{v}'$ and the reconstructed photon direction $\hat{v}$, given by $\theta = \arccos(\hat{v} \cdot \hat{v}')$. From the θ distribution the 68% and 95% event containment angles (i.e. the 68% and 95% quantiles of the θ distribution) are estimated. The figure shows these distributions, weighted over the acceptance, as a function of the photon energy for P8R3_SOURCE_V3 events converting in the front/back section of the TKR and for all the events. In the low energy range the PSF is governed by the multiple Coulomb scattering in the TKR, which affects the trajectories of electrons and positrons produced in the gamma ray pair-conversion. Indeed, at low energy the distributions tends to decrease with energy, resembling the 1/E dependence of the multiple scattering angle. At high energy, the multiple scattering becomes negligible, but the PSF is limited by the finite spatial resolution of the SSDs in the TKR.

The figure shows the energy resolution ΔE/E, defined as the 68% containment of the reconstructed photon energy (divided by the true energy E), as a function of energy, for P8R3_SOURCE_V3 photons. It can be observed that the energy resolution is better than ~ 15% over a wide energy range. At low energies the resolution is limited due to the high fraction of energy losses in the TKR, while in the high-energy range it worsens because of the partial containment of the particle showers in the CAL and the saturation of most of its crystals.

https://www.slac.stanford.edu/exp/glast/groups/canda/lat_Performance.htm

More on likelihood

In the case $k > 1$ (k = number of parameters to fit), it is possible to construct a confidence region in the parameter space such that the true parameters α_k are contained within the region with a given probability. This region approaches a m-dimensional hyperellipsoid in the large sample limit. It can be shown that the confidence region with the confidence level $1 - \gamma$ can be constructed by finding the values of α_k for which the log-likelihood decreases from its maximum value by the quantity $Q\gamma/2$, where $Q\gamma$ is the quantile of order $1 - \gamma$ of the χ^2 distribution with m degrees of freedom:

$$\ln \mathcal{L} = \ln \mathcal{L}_{max} - \frac{Q_\gamma}{2}$$

$$\mathrm{TS} = 2 \ln \left(\frac{\bar{\mathcal{L}}}{\bar{\mathcal{L}}_0} \right) = 2(\ln \bar{\mathcal{L}} - \ln \bar{\mathcal{L}}_0)$$

$\ln\bar{\mathcal{L}}$ is the maximum log-likelihood corresponding to the model F', depending on the m parameters α_k, while $\ln\bar{\mathcal{L}}_0$ is the maximum log-likelihood corresponding to a model F'_0 depending on h parameters α_k, with $h < m$. For example, F'_0 could be the model obtained by fixing $m - h$ parameters of the model F'. The Wilk's theorem states that the TS-value is asymptotically distributed as a χ^2 with $m - h$ degrees of freedom. The full model F' could include a gamma-ray source which in the model F'_0 is not present, i.e. the parameter of interest would be the flux of the putative source, while in the null hypothesis this flux would be zero. In this case, the TS value expresses the significance of the source. In particular, if $m - h = 1$, one finds that $\sqrt{TS}$ is approximately the significance expressed in σ units. If $TS \geq 25$, the significance of the source is $\geq 5\sigma$, and one claims that the source has been detected. If no detection is found, an upper limit can be set on the source flux. Let us assume, for example, that the flux of the putative source is modeled as a reference (fixed) flux multiplied by a normalization parameter C. In this case, the parameter of interest is C, which in the null hypothesis is equal to zero, and finding the upper limit on the source flux means finding it for C: a likelihood scan is performed varying the normalization parameter, until a decrease in log-likelihood corresponding to the desired confidence level is reached. For example, a decrease in log-likelihood of 2.71/2 = 1.35 corresponds to a 95% C.L. upper limit.

Fermi Science Tools

Events files, or FT1, contain the list of the parameters of each photon event, organized in columns. *Spacecraft files*, or FT2, contain information about the position, the orientation and the livetime history of *Fermi.*

Data selection: the tool **gtselect** allows for selecting the set of events which are best recommended for the science analysis to perform. In general, these events are selected according to different selection criteria (cuts), which depend on the analysis being performed. A first cut is applied to select photons from a given region in the sky, within a given energy range and a given time interval. A second cut regards the selection of photons belonging to a given class and type. Another cut is based on the maximum zenith angle, which is the angle between the incoming photon direction and the direction perpendicular to the Earth's surface. Usually, photons with a too large zenith angle are discarded, in order to avoid the bright contamination of gamma rays produced in the interactions of CRs with the outer layers of the Earth's atmosphere (*Earth limb*).

Calculation of the Good time intervals (GTIs): GTIs are time intervals in which the data can be considered valid for the analysis and are calculated by the tool **gtmktime** using the spacecraft quantities contained in the FT2 file, like for example the position and orientation of the spacecraft as a function of time. gtmktime applies a logical filter on these quantities, based on specified cuts. For example, it descards time intervals when the spacecraft is in the South Atlantic Anomaly. Then, it combines (logical "and") the calculated GTIs with the time intervals in the event data file, and it removes from the file all time ranges outside the GTIs. GTIs are then used by other tools to correctly calculate the exposure of the LAT.

Livetime and exposure: the livetime is the time when the spacecraft observed each position of the sky. This calculation is performed by the tool **gtltcube**, which calculates the livetime as a function of the sky direction and of the off-axis angle. The dependence on the off-axis angle is important since the IRFs depend on this angle. The following step is to compute the exposure for the region of the sky under analysis, which has to be divided into pixels of arbitrary dimensions. The exposure is calculated by folding the livetime computed with gtltcube with the effective area of the instrument parameterized by the IRFs. The tool that calculates the exposure is called **gtexpcube2**.

Fermi Science Tools

The last step prior to perform the fit is the evaluation of the observed and expected counts for each pixel and energy bins. The observed counts are obtained with the tool **gtbin**, which realizes a count map of the observed photons in 3-D, where two dimensions are given by the two spatial coordinates and the other dimension is given by the energy binning.
The expected counts are obtained by folding the model flux of the region of the sky under investigation with the exposure and the IRFs. The model flux is given by the sum of different sources, which are described in the XML format. Each source in the XML file is parameterized as the product between a spatial and a spectral factor. The list of the spatial models and an up-to-date list of the spectral models available are described in the *Science Tools* documentation (https://fermi.gsfc.nasa.gov/ssc/data/analysis/scitools/source_models.html#spatialModels). In addition to the source models, the XML model file includes models of the Galactic and extragalactic diffuse emission, which contribute to the background and are therefore needed for a proper fitting of the source parameters.

The first step to obtain the expected number of counts is to perform a spatial integration, consisting in multiplying the spatial model by the exposure previously calculated and folding the product with the LAT PSF. This task is fulfilled for each pixel into which the region of the sky under investigation has been divided, and for different values of the energy. This integration is performed by the tool **gtsrcmaps** independently for each source in the model.

The second step is to perform an integration over the energy. This integration consists in multiplying the quantity previously obtained by the spectral factor of the model and folding the product with the LAT energy dispersion function.

The likelihood fit is performed by the tool **gtlike**, which uses the observed and expected counts to define the log-likelihood, whose maximum is found using minimization algorithms, such as MINUIT. gtlike returns as output the best-fit values of the model parameters and their statistical uncertainties, which are stored in a XML file identical to the input one but with the updated values and the corresponding errors. For each source in the model, the tool gtlike also returns the maximum log-likelihood value, which is used to determine the TS for the source with respect to a model from which the same source is eliminated (null hypothesis).

Comparison between asteroids and Moon flux

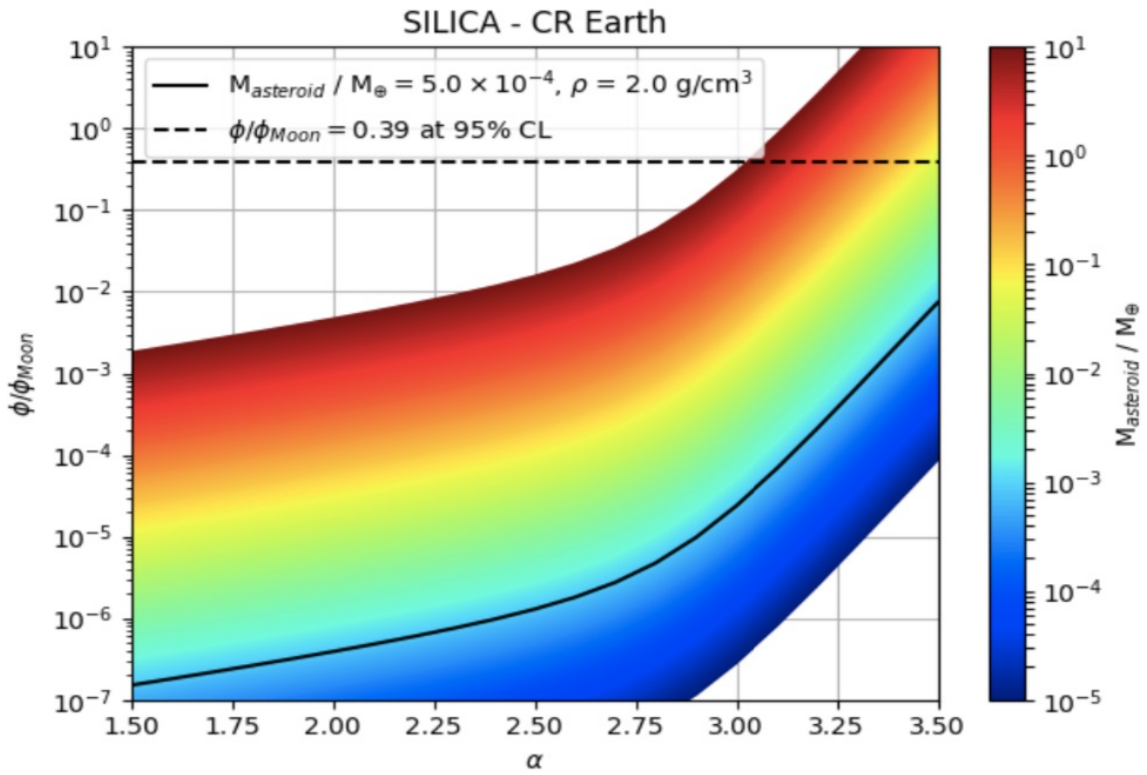

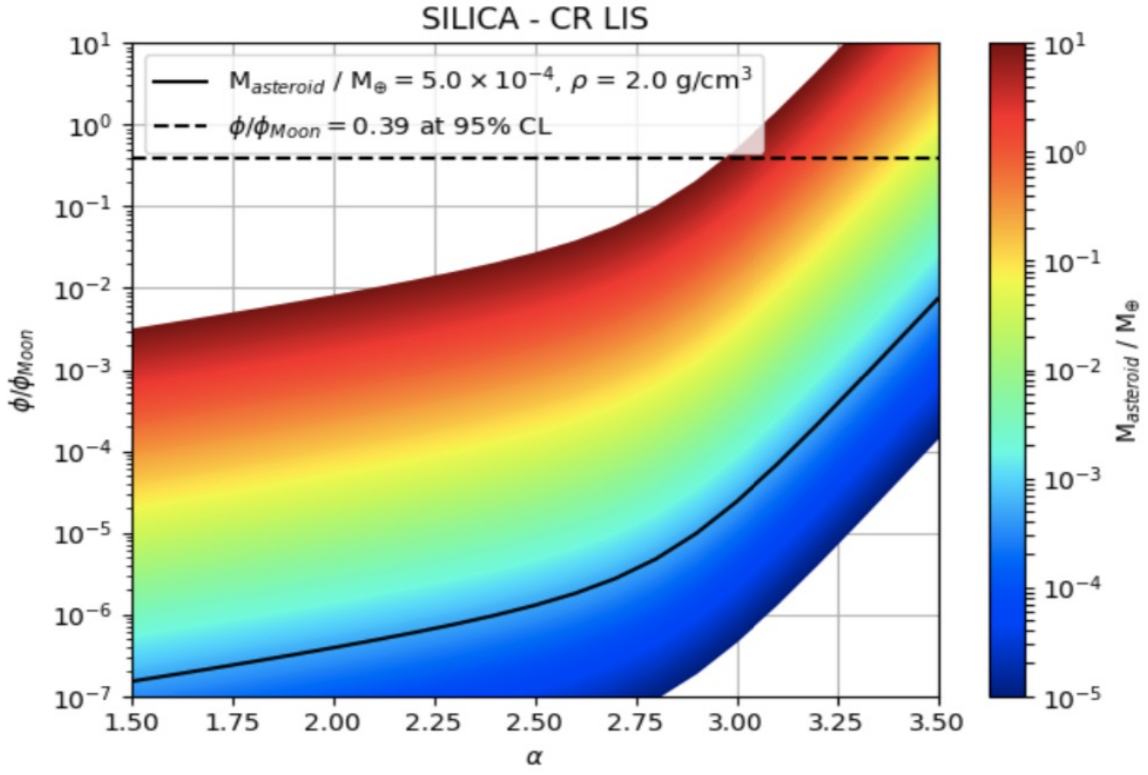

The gamma-ray Moon over an entire solar cycle

- In M. Ackermann et al., 2016, the Moon gamma-ray flux was reconstructed in the first 7 years of *Fermi*-LAT operation
- In this work, the first 14 years *Fermi*-LAT data (Aug 2008 – Jun 2022) have been used
  - This period exceeds the duration of a solar cycle
  - Pass 8 P305 dataset, SOURCE events (FRONT and BACK), with energy > 10 MeV

May 2011 – Nov 2013

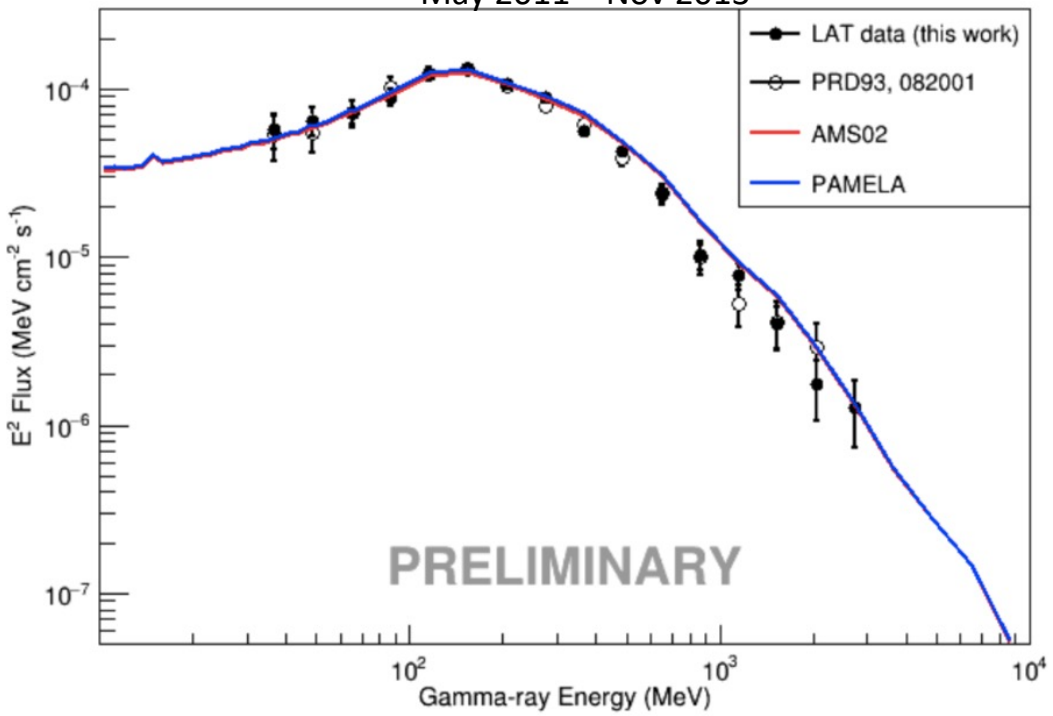

AMS data: M. Aguilar et al., 2015
PAMELA data: M. Martucci et al., 2018, O. Adriani et al., 2011

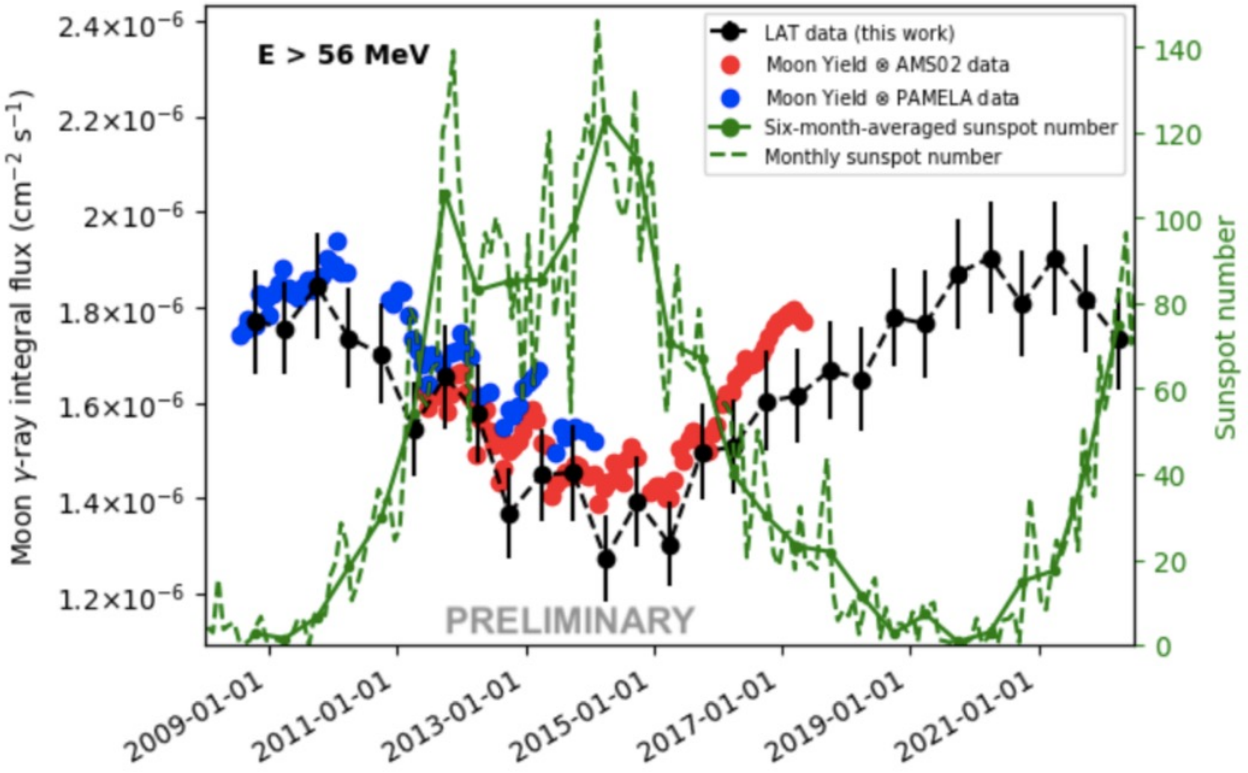

AMS data: M. Aguilar et al., 2018
PAMELA data: M. Martucci et al., 2018, O. Adriani et al., 2011, 2013
Sunspot number: SILSO WDC (http://www.sidc.be/silso/)